Cretaceous Research 154 (2024) 105736

Contents lists available at ScienceDirect

Cretaceous Research

journal homepage: www.elsevier.com/locate/CretRes

Magnetic surveying as a proxy for defining cyclicity in thick sedimentary fillings: Application to the Cretaceous Cameros Basin (N Spain)

Antonio M. Casas, Arsenio Muñoz [1], Alberto Tella, Carlos L. Liesa*

Departamento de Ciencias de la Tierra-Geotransfer, Instituto de Ciencias Ambientales, IUCA, Facultad de Ciencias, Universidad de Zaragoza, Pedro Cerbuna 12, 50009 Zaragoza Spain

ARTICLE INFO

Article history:
Received 4 April 2023
Received in revised form
25 September 2023
Accepted in revised form 1 October 2023
Available online 7 October 2023

Keywords:
Cyclostratigraphy
Magnetic surveying
Magnetic susceptibility
Sedimentary cyclicity
Cameros basin

ABSTRACT

This work proposes the application of magnetic surveying to the study of cyclicity in sedimentary basins. This application is favoured by the particular bed attitude/topography relationships found in the eastern sector of the Cretaceous Cameros Basin, N Spain. Both the measured total magnetic field (after diurnal correction) and the vertical magnetic gradient, provide a profile (14 cm separation between measurements, in average) of the short-wavelength magnetic anomalies associated with the sedimentary sequence. These anomalies depend on the magnetic susceptibility (dominant for low Koenigsberger ratios, a common scenario in sedimentary rocks), and the magnetic remanence (whose orientation is fairly constant in remagnetised basins) of the different sedimentary units. The comparison with direct measurements of magnetic susceptibility (in the field and in the laboratory) provided a successful double-check. The cyclostratigraphic analysis of magnetic profiles of this 6 km-thick series indicates the existence of cycles of 405 kyr (long eccentricity) and 100–125 kyr (short eccentricity), as well as other lower and higher frequency cycles. Cycles with similar, but slightly different, periodicities are the result of different sedimentation rates (mean of ~0.2 mm/yr, with values ranging between ~0.1 and ~0.36 mm/yr). These results provide and indirect method for dating the basin fill, between the Tithonian–Berriasian boundary and the basalmost Albian (~143.2–~112.6 Ma), and impose new constraints for basin evolution. The results obtained open a promising field for quick and reliable determination of magnetic properties and cyclicity in thick sedimentary sequences.

1. Introduction

Magnetic properties are being extensively used for the determination of sedimentary cycles, the characterization of changing sedimentary environments and the indirect dating of sedimentary series (Schlicht et al., 1998, 1999; Boulila et al., 2008; Kodama et al., 2010; Koptíková et al., 2010; Gunderson et al., 2013; Oliva-Urcia et al., 2016; Brocke et al., 2017). Magnetic susceptibility is relatively easy to determine and its measurement is quick, non-destructive and low-cost. It can be related to the iron content of the rock and hence to climatic conditions during deposition (Stage, 2001; Vandenberghe et al., 2004; Oliva-Urcia et al., 2016; Brocke et al., 2017). The study of magnetic susceptibility has been successfully used in recent years to define climatic sedimentary cycles based on two premises: (i) the response of the iron content in sediments to climatic changes (higher solution/precipitation rates during humid/warm periods and lower rates during dry/cold ones) and (ii) the coupling between the iron content and the magnetic susceptibility. Numerous examples have proved the usefulness of this technique both in ancient and modern sediments (e.g., Schlicht et al., 1999; Ellwood et al., 2000; Da Silva et al., 2013; Kodama and Hinnov, 2014; Oliva-Urcia et al., 2016; Brocke et al., 2017; Liu et al., 2020; Pfeifer et al., 2020; Powers et al., 2020; Omar et al., 2021; Golovanova et al., 2023).

Measurements of magnetic susceptibility can be done (i) directly in the field with a hand-held susceptibility metre, combined or not with GPS (integrated in some of the available devices), or (ii) in the laboratory, through collection of samples that are analysed by means of a susceptibility bridge, from standard

* Corresponding author.
E-mail address: carluis@unizar.es (C.L. Liesa).
[1] In memoriam.

https://doi.org/10.1016/j.cretres.2023.105736

cylindrical paleomagnetic specimens (11 cm^3), cubic samples (ca. 8 cm^3), or irregular samples (Jelinek, 1977; Gracia-Puzo et al., 2021 and references therein). In both cases, the representativeness of the data is achieved by (i) measuring several points of the same bed (or taking a sufficient number of samples), and (ii) by choosing a convenient spacing between sites, depending on the frequency of the investigated cycles.

Magnetic surveying is based upon the detection of anomalies of the Earth's magnetic field caused by underground bodies with particular magnetic properties. The magnetic susceptibility and remanence of these geological bodies, their depth and volume, and their geometry and orientation in relation to the Earth's magnetic field, are the factors that control the generated magnetic anomalies. These anomalies can be measured at surface by means of a magnetometer, even when the target bodies are covered by surficial units. The induced magnetization depends on the magnetic susceptibility and the external magnetic field. In mid-latitudes of the northern hemisphere, magnetic anomalies associated with high-susceptibility bodies and exclusively controlled by induced magnetization show a dipolar geometry, with a positive peak to the South and a negative segment to the North (see, e.g. Hinze et al., 2013). The pattern of magnetic anomalies created by a particular body can be more complicated when its remanent magnetization (a three-component vector) is high. The orientation of this vector relative to the present-day magnetic field can vary according to the period of acquisition of the remanent magnetization (normal or reverse magnetic field), large-scale movements linked to continental evolution, and local rotations associated with folding and thrusting (see, e.g. Calvín et al., 2014).

The definition of a particular magnetic anomaly can be achieved either through continuous measurements (i.e. by means of a fluxgate magnetometer, see e.g. Telford et al., 1990; Kearey et al., 2002) or through discrete measurements, usually by means of a proton magnetometer (Everett, 2013). In the latter case, common-use proton magnetometers with Overhauser effect (Hrvoic, 1990; Liu et al., 2017) provide high measurement frequency (up to 5 measurements per second) and precision (less than 0.5 nT). However, instabilities derived from the movement of the sensor and unavoidable noise (resulting from surface debris, soils developed over the target units, anthropogenic noise, etc…) commonly limit the accuracy of measurements to 1–2 nT.

Magnetic surveying is a routine tool for many geological and archaeological purposes (Milsom, 2003; Butler, 2005; Burger et al., 2006; Witten, 2006; Gadallah and Fisher, 2008; Oswin, 2009; Griffiths and King, 2013; Dentith and Mudge, 2014; Florsch et al., 2018; Eppelbaum, 2019, among others). It is a quick and easy-to-use geophysical technique that does not need time-consuming, post-survey processing. The best results are achieved when the targets have high susceptibility and/or remanence (i.e. volcanic rocks or ore bodies). Nevertheless, modern, proton-precession magnetometers provide good results in practically all environments, even when contrasts of susceptibility between bodies are not extremely high (see e.g. Pueyo-Anchuela et al., 2016). Direct or inverse modelling of geological bodies in the shallow subsurface provide a good approximation to their geometry and to the double-checking of their magnetic properties (see e.g. Hinze et al., 2013).

In this work, we relate the results of magnetic surveying with the magnetic properties of sedimentary sequences, and interpret them (in particular the analysis of short-wavelength magnetic anomalies) in terms of sedimentary cyclicity associated with climatic forcing. The target of our study is the eastern Cameros Cretaceous Basin (Iberian Chain, N Spain), where a 6000 m-thick sedimentary sequence, showing an overall homogeneous dip, is exposed. The studied sedimentary units include syn-rift sediments deposited in different environments and showing distinct magnetic properties (Villalaín et al., 2003; Del Río et al., 2013; García-Lasanta et al., 2017). The low magnetic noise and the optimal orientation of beds and slopes contribute to the good results obtained.

2. Geological background

The Cameros Massif constitutes the northwesternmost sector of the Iberian Chain, an intraplate mountain building located in the central-northern part of the Iberian microplate (Fig. 1). The Iberian Chain resulted from the inversion during the Cenozoic of several extensional sedimentary basins developed since the Triassic until the Late Cretaceous (Liesa et al., 2018). The Cameros Basin is the most important of these Mesozoic basins, totalling 9 km in thickness (Muñoz-Jiménez and Casas-Sainz, 1997; Casas-Sainz and Gil-Imaz, 1998; Mata et al., 2001). The syn-rift sedimentary sequence is superbly exposed in the hangingwall of the 150 km-long Cameros–Demanda thrust (Casas-Sainz, 1993; Guimerà et al., 1995). This structure superposes the Paleozoic and Mesozoic rocks onto a 2.5 to 4 km-thick pile of the Cenozoic deposits of the Rioja Trough (Muñoz-Jiménez and Casas-Sainz, 1997). The central-eastern part of the inverted Cameros Basin is dominated by a E–W to NNW–SSE-trending syncline (Casas et al., 2009), whose thickened southern limb (tenfold relative to the northern limb) shows a homogeneous dip (between 20 and 60°) towards the N to ENE (Fig. 1). Although this syncline was formed during the Cenozoic shortening (García-Lasanta et al., 2017), some syn-extensional geometries are preserved, especially in its northern limb (Guiraud and Séguret, 1985; Casas-Sainz, 1993; Casas-Sainz and Gil-Imaz, 1998; Casas et al., 2009).

The filling of the Cameros Basin consists of Triassic, Jurassic and Cretaceous series of marine and continental origin. The Lower and Middle Triassic crop out in the eastern and western basin borders (see, e.g. López-Gómez et al., 2019, and references therein). The Upper Triassic (Keuper facies), consisting of shales and gypsum, crops out throughout the northern basin border and acted as an effective *décollement* for the Jurassic and Cretaceous cover, that were completely detached from the underlying units both during the extensional (Soto et al., 2007) and the compressional (Casas-Sainz and Gil-Imaz, 1998) stages. The Jurassic consists of marine marls and limestones and shows a homogeneous thickness of about 1000 m throughout the basin. The Lower Cretaceous is the most important part of the syn-rift sequence, with 8000 m of continental deposits (Tischer, 1966a, 1966b; Guiraud and Séguret, 1985; Mas et al., 2002; Clemente, 2010). This syn-rift sequence is divided into five lithostratigraphic groups (Tischer, 1966): Tera, Oncala, Urbión, Enciso and Oliván, deposited between the Tithonian and the Albian (Clemente, 2010; Martín-Chivelet et al., 2019). In this work we have focused on the three younger units (Fig. 1). The Urbión Group is dominantly detrital (quartzitic sandstones and shales, Mata-Campo, 1997). The Enciso Group consists of limestones, marls and thinner detrital units of lacustrine and deltaic origin (Angulo and Muñoz, 2013). Finally, the Oliván Group is detrital, and consists of alternating sandstones and shales. All the syn-rift units underwent a low-grade metamorphic stage at ca. 100 Ma (Goldberg et al., 1988; Mata et al., 2001; Casas et al., 2012; Del Río et al., 2013; Omodeo-Salé et al., 2014). This process was probably associated with the wholesale remagnetization, chemical in origin, of the pre-rift and the syn-rift sequences (Villalaín et al., 2003; Casas et al., 2009; García-Lasanta et al., 2017).

The Cameros Basin has been the subject of numerous studies, including magnetic surveying, anisotropy of magnetic susceptibility and palaeomagnetism (Gil-Imaz et al., 2000; Villalaín et al., 2003; Casas-Sainz et al., 2009; Del Río et al., 2013; García-Lasanta et al., 2013, 2014, 2017). The magnetic properties of the rocks of the syn-rift sequence are therefore well known (Fig. S1 in

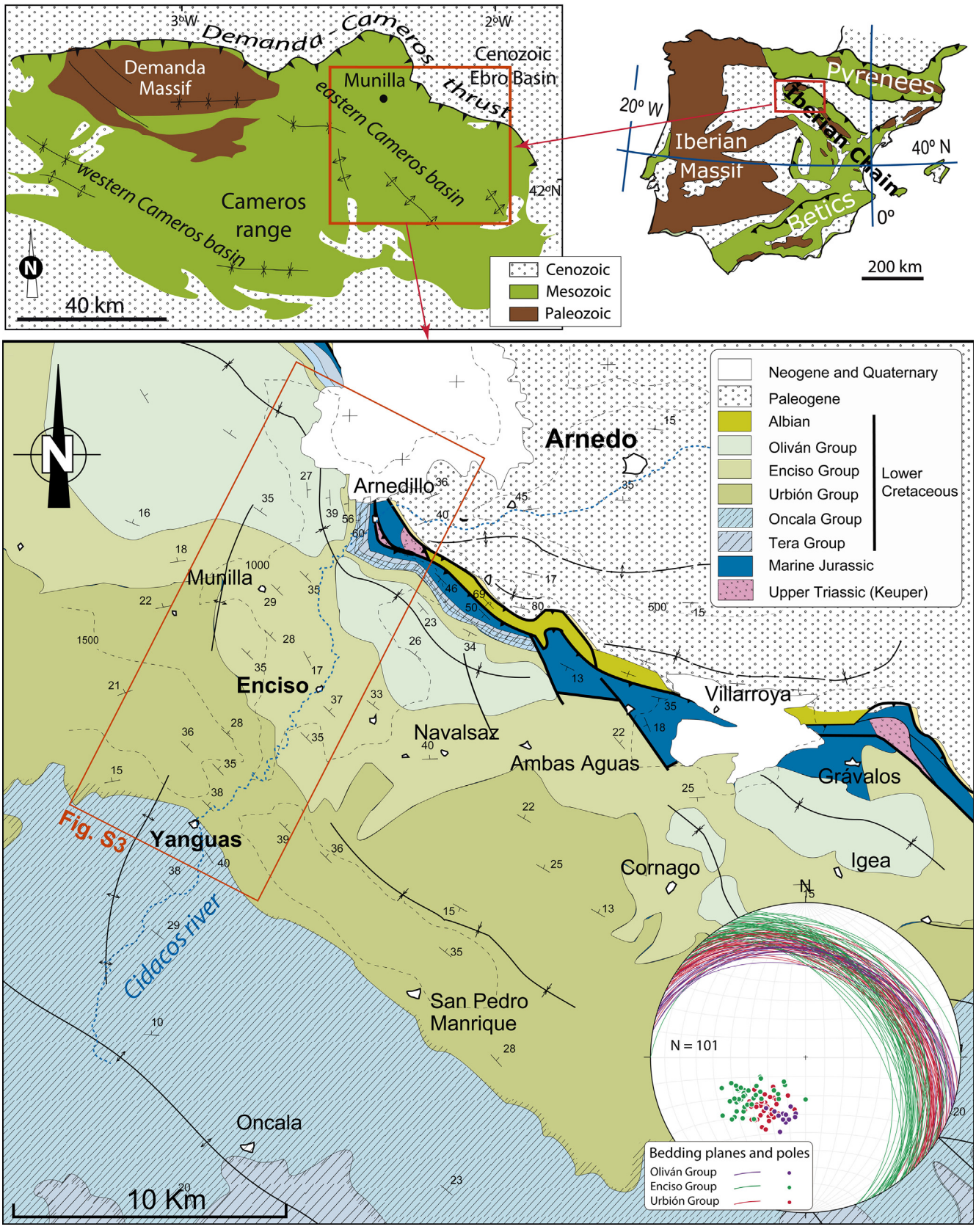

Fig. 1. Location and geological sketch of the eastern part of the Cretaceous Cameros Basin. Stereoplot (lower hemisphere, Wulf net) shows the bedding orientation.

Supplementary file). Their magnetic remanence is between 0.15 and 50 mA/m and their magnetic susceptibility ranges between -28×10^{-6} SI and 552×10^{-6} SI (Gil-Imaz et al., 2000; Villalaín et al., 2003; Del Río et al., 2013; García-Lasanta et al., 2013, 2014, 2017). The extreme values of magnetic susceptibility (both high and low) correspond to the Urbión Group. The Enciso Group shows magnetic susceptibility values between 57×10^{-6} SI and 519×10^{-6} SI (most of them between 100×10^{-6} SI and 350×10^{-6} SI, García-Lasanta et al., 2014). In the Oliván Group susceptibility varies between -26×10^{-6} SI and 280×10^{-6} SI. Magnetic remanence and magnetic susceptibility show a positive correlation in the different types of rocks (García-Lasanta et al., 2017) and their Koenigsberger ratios vary between 0.3 and 13, with a median of 1.3 and a mode between 0 and 1. Similar results (and variability) have also been obtained in other remagnetised basins (Casas-Sainz et al., 2023). Since all the syn-rift series was remagnetized at the end of the Early Cretaceous, the strong, characteristic component of the remanence is normal (Villalaín et al., 2003). Furthermore, the dip of beds is also relatively homogeneous. This makes easier the task of vector decomposition of the induced and the remanent magnetization, since both vectors show similar orientations. On the other hand, we have not found significant changes of magnetic susceptibility (or local magnetic anomalies associated to them) between the weathered and fresh rocks, thus implying that the possible weathering of pyrite (appearing as fresh crystals in the road cuts) and other minerals has not a strong influence in the averaged measurements.

The magnetic mineralogy in the different units is as follows. In the fluvial Urbión Group, the carriers of the magnetic susceptibility are (i) haematite and very minor amounts of magnetite and sulphides (García-Lasanta et al., 2014) as ferromagnetic (s.l.) minerals and (ii) phyllosilicates, mainly chlorite (of diagenetic origin, Mata et al., 1991; Barrenechea et al., 2000; Mata-Campo and López-Aguayo, 2002), as paramagnetic minerals. The phyllosilicates are only present in the pelitic units. The Enciso Group contains (i) sulphides and magnetite as ferromagnetic phases and (ii) chlorite as the main paramagnetic phase (García-Lasanta et al., 2013). Finally, the Oliván Group contains (i) chlorite as the main paramagnetic phase in its upper part, whereas (ii) in its lower part, haematite is considered to be the main carrier of magnetic susceptibility (García-Lasanta et al., 2017).

Cyclostratigraphic studies are relatively scarce in the Cameros Basin. Spectral analysis based on different palaeoclimatic proxies, such as lithology, colour (L*, a*, and b* indices), field-measured magnetic susceptibility or mineralogy (percentage of calcite, dolomite or total carbonate), has focused specially on the lacustrine and fluvial deposits of the Enciso Group (e.g., Doublet et al., 2003; Doublet, 2004; Angulo and Muñoz, 2013; Hernán, 2018; Muñoz et al., 2020, 2021). The sedimentary cyclicity inferred from these studies has been associated with a climatic control of orbital origin referred to the Milankovitch cycles (Milankovitch, 1941), including long and short eccentricity, obliquity and precession.

3. Methodology

3.1. Magnetic survey

Two kinds of measurements were taken in this work: vertical magnetic gradient and total magnetic field. The total magnetic field is measured at a distance of 1.5 m above the topographic surface, to avoid influence from small surficial elements. Data must be corrected according to the diurnal variations of the Earth's magnetic field. The vertical magnetic gradient is the difference between measurements with sensors located at 1.5 m and 2 m from the surface (Fig. S2). This kind of measurement enhances the influence of near-surface elements, and is of common use in archaeology (Smekalova et al., 2008; Oswin, 2009; Florsch et al., 2018). The vertical gradient is not influenced by diurnal changes or deep magnetic sources (provided that the distance between the two sensors is small). The comparison between the two measurements (total magnetic field and vertical gradient) gives an idea of the depth to the source of the magnetic anomalies. Since in this work only the high-frequency, short-wavelength signals are retained, the coincidence between the results obtained from the vertical gradient and the total magnetic field is a test for assessing the quality of the results.

The equipment used was a GSM-19 proton magnetometer (Gemsys, Canada) with Overhauser effect, using a sampling frequency of 0.5 s, with a precision of 0.1 nT (Fig. S2). Because of the movement of the sensors of the rover magnetometer, the actual accuracy (repeatability) obtained was 1–2 nT (Fig. S2). Diurnal changes were controlled with a base magnetometer (PMG-1, GF Instruments, Czech Republic), located at a fixed point (Fig. S3), with measurements every 20 s, what allowed us to make correlations between profiles surveyed during different days.

In the regular survey of the Urbión, Enciso and Oliván groups, the magnetic data (total field and gradient) were taken along eight profiles, with NNE–SSW to ENE–WSW directions, more or less parallel to the Cidacos River (profiles labelled Ur1, Ur2, Ur3, En1, En2, En3-Ol1, Ol2, and Ol3 in Fig. S3). Measurements of attitude of beds were taken every 50–100 m of the sedimentary pile, and fault traces were determined from detailed mapping. When possible, profiles were perpendicular to bedding strike, along south-dipping slopes, i.e. the scarp slope in the landforms associated with the dipping strata (Fig. S2B). Measurements along North-dipping slopes (dip slope of the cuestas) are more or less parallel to bedding and were not used for constructing the profiles, what created in some cases small gaps. Some of the profiles were surveyed forward and backwards along the pathway, obtaining in general cleaner results when walking in the downdip direction. During processing, some of the profiles were merged in order to obtain more continuous logs. Correlation between profiles was carried out by combining fieldwork and analysis of high-resolution (0.5 m/pixel) aerial orthoimagery (from the Spanish Geographical Institute, IGN and Google-Earth). Several gaps and overlaps between profiles were identified. The overlapping parts of the profiles were not analysed.

In the Urbión Group two more profiles, more irregular in their tracing and not strictly perpendicular to bedding (Fig. S2), were surveyed. The first one (UrL) follows forest roads and covers the lower part of the unit. The second one (UrU) follows an alternative path, parallel to Ur2, and covers its upper part. The objective of these surveys is to check the repeatability of the results under different outcrop and pathway conditions (this point will be discussed below). Magnetic survey data were processed by means of the GEMlink software (Gemsys, Canada).

A magnetic susceptibility log was also acquired in the Urbión Group from the Yanguas locality to the Enciso dam (Fig. S3), along the fresh cuts of the main road. Measurements were taken with a KT-20 (Georadis, Terraplus, Canada) susceptometer with an integrated GPS. Three to eight measurements were taken in 357 sites (average spacing ca. 8 m). Magnetic susceptibility was also checked in the laboratory by means of a KLY3-S (Kappabridge) susceptibility metre (AGICO, Czech Republic).

3.2. Transforming magnetic data to stratigraphic magnetic profiles

The data obtained in the magnetic surveys (longitude, latitude, elevation, total magnetic field and vertical magnetic gradient) were converted into a stratigraphic magnetic profile. Profile data were

projected onto a straight line perpendicular to bedding (beginning at a reference point whose height h in the stratigraphic log is equalled to 0) according to the equation:

$$h = u_x*(x_i - x_0) + u_y*(y_i - y_0) + u_z*(z_i - z_0)$$

where: u_x = sin(strike)*sin(dip), u_y = cos(strike)*sin(dip), and u_z = cos(dip) are the components of the unit vector perpendicular to bedding (characterized by its strike and dip) in each profile or each segment of the profile, x_0 and y_0 are the easting and northing (UTM coordinates) of the reference point used as the origin for the magnetic profile, and z_0 its elevation, and x_i and y_i the coordinates of each measuring point and z_i its elevation.

The scalar product of the two vectors (h) provides the linear distance perpendicular to bedding from the origin (x_0, y_0, z_0) to each measuring point. This allows establishing magnetic logs that correspond bed-to-bed to stratigraphic logs. Careful photointerpretation must be done in advance, in order to avoid faults cutting across, and displacing the series, what could lead to subtractions or repetitions of parts of the stratigraphic sequence.

3.3. Magnetic modelling

2.5D magnetic modelling was done by means of the GravMag software (Pedley et al., 1993) of the British Geological Survey. This program provides the theoretical magnetic field created by a geological body (a polygon in cross-section) with a particular geometry and distinct magnetic properties (magnetic susceptibility and remanence) and located at a particular latitudinal position. The magnetic anomaly obtained by means of forward modelling can be compared with the actual anomaly obtained in the survey. Magnetic modelling is usually done in 2D (in cross-section), but the length of the polygons (prisms in 2.5D) perpendicular to the plane of the section is also an input for the model.

3.4. Cyclostratigraphy

Cyclostratigraphy is based on the recognition of astronomically forced climatic changes in sedimentary sequences. Variations of the Earth's orbital parameters (long an short orbital eccentricity, axial tilt obliquity and precession) affect the amount of insolation on the Earth and generate climatic, biological and oceanographic fluctuations with different duration (Milankovitch cycles, Hinnov, 2013) and can be preserved in the sedimentary record. The duration and reconstruction of Milankovitch cycles during the Early Cretaceous has been based in the numerical model by Laskar et al. (2004, 2011).

We used the changes in the total magnetic field, the vertical gradient and the changes in the magnetic susceptibility to define orbitally forced variations. The values of these parameters were interpolated to the value of the mean sampling interval in each series. Subsequently, the general trend was eliminated using a LOWESS smoothing model (Cleveland, 1981). The characterization of the frequency content of the processed series was established by means of the Multi-taper method (MTM), power spectral analysis (Thomson, 1982). The calculated spectra were verified with respect to robust red noise models at different confidence levels (90%, 95%, 99%, Mann and Lees, 1996). The analysis of frequency cycles was performed using the Evolutionary Spectral Analysis methodology (Kodama and Hinnov, 2015), with a 300 m window, obtaining the evolutionary Fast Fourier Transform (FFT) spectrogram. A smoothing Gaussian filter was used to characterize the low frequency cycles. All these procedures were performed using the Acycle v. 2.4.1 software (https://github.com/mingsongli/acycle) (Li et al., 2019). The MTM F-ratio test was used to determine significant harmonic lines. The astronomical target frequencies are based in the ETP values of the La2010 astronomical solution periodogram calculated for the Early Cretaceous (Laskar et al., 2011): long orbital eccentricity (405 kyr), short orbital eccentricity (100 kyr; 125 and 95 kyr modes), obliquity (37.2 kyr) and precession (22.4 kyr and 18.2 kyr). These Milankovitch cycles follow approximately the 1:4:11:20 relation, and served as a preliminary test for astronomical frequencies in the magnetic logs (e.g., Laskar et al., 2004). Results have been anchored to the most recent Geological Time Scale (GTS2020) established for the Cretaceous Period (Gale et al., 2020).

4. Results

4.1. Magnetic profiles

4.1.1. Regular magnetic survey

The eight logs measured in the regular magnetic survey total ~6312 m and cover almost completely the stratigraphic series under investigation (Figs. S3, 3 and Table 1). The total magnetic field and magnetic gradient measurements are comparable and correlatable (Figs. 2 and 3). Correlation of sections using satellite orthoimages allowed us to recognize (i) two significant overlaps: ~180 m between the Ur2 and Ur3 profiles and ~160 m between the En3-Ol1 and Ol2 profiles, and (ii) three minor gaps between the Ur1 and Ur2 (~30 m), Ur3 and En1 (~30 m), and Ol2 and Ol3 (~50 m) profiles. These gaps coincide with the dip slopes of cuestas (north-dipping beds underlying a north-dipping slope, Fig. S3). All in all, the investigated Cidacos section in the eastern Cameros Basin is ~6070 m thick (2445 m, 1108 m, and 2517 m for the Urbión, Enciso and Oliván groups, respectively). Our data cover about 98% (5960 m) of the sedimentary succession (Liesa et al., 2023).

The total magnetic field (after diurnal correction) profiles indicate the influence of a long-wavelength (low-frequency) anomaly (Fig. 3I) related to an underlying high-susceptibility body, probably a large-scale basic dyke related to Triassic extension (Del Río et al., 2013). Because of its wavelength, this is not reflected in the gradient profiles and can be easily filtered in order to enhance short-wavelength anomalies related to climatic forcing.

The base of the Urbion Group (Ur1 log) is characterized by relatively strong anomalies, whose amplitudes reach 25 nT and whose wavelengths are on the order of several metres (Fig. 3A). Along the profile there are higher frequency anomalies, with amplitudes of 5 nT. The Ur2 profile is more irregular and shows three different sectors separated by anomalies with amplitudes of 20 nT (Fig. 3B). The overall trend of increasing magnetic field towards the northeast is consistent with the previously mentioned, large-scale Cameros magnetic anomaly (Del Río et al., 2013). In each of the three segments of the profile, short-wavelength anomalies with amplitudes of 2−5 nT are also common. Wavelengths of anomalies increase towards the upper part of the series. The Ur3 profile shows two different parts (Fig. 3C), below and above the 800 m level, a limit that coincides with a change in colour, outcrop aspect and vegetation canopy (thicker for higher pelite content). Below the 800 m level, the profile is more regular than Ur2, and short-wavelength, low-amplitude anomalies are the dominant feature. Above 800 m, anomalies show again higher amplitude, reaching 20 nT, and also longer wavelength.

Profiles En1 and En2, corresponding to the Enciso Group, show similar patterns, with long-wavelength anomalies (reaching 5 nT in amplitude) and a general ascending trend towards the NE, i.e., upwards in the stratigraphic series (Fig. 3D,E). These long-wavelength anomalies are hardly detected in the gradient profile, thus indicating a deeper source. Profile En2 shows a more homogeneous aspect, with clearer and shorter wavelength ruptures in metres 70, 210, and 300.

Table 1
Magnetic (total magnetic field and vertical magnetic gradient) and magnetic susceptibility logs surveyed in the eastern Cameros Basin (see location in Fig. S3), showing the stratigraphic thickness of magnetic profiles and the estimation of gaps and overlaps between profiles. The cyclostratigraphic profiles derived from magnetic logs, by division or union thereof, are also shown.

Unit	Magnetic log	Stratigraphic thickness surveyed	Cyclostratigraphic profiles	Stratigraphic thickness
Magnetic survey (total magnetic field and vertical magnetic gradient)				
	Regular magnetic survey (for constrain the complete stratigraphic series)			
Oliván Group	**Oliván 3 (Ol3)**	965 m	**Ol3**	510 m (upper part Ol3)
			Gap of 110 m, only for the total magnetic field measurements (because of wind turbines)	
			Ol2	370 m (lower part Ol3)
	Gap of 50 m (no profile)			Gap of 50 m
	Oliván 2 (Ol2)	954 m		954 m (the complete profile)
	Overlap of 162 m (898–1060 m of En3-Ol1 profile was not analysed)			
	Enciso 3-Oliván 1 (En3-Ol1)	1060 m	**Ol1**	523 m (from 375 to 898 m)
Enciso Group			**En3**	350 m (from 25 to 375 m)
	Enciso 2 (En2)	380 m	**En2**	380 m (the complete profile)
	Overlap of 10 m			
	Enciso 1 (En1)	358 m	**En1**	358 m (the complete profile)
	Gap of 30 m (no profile)			
Urbión Group	**Urbión 3 (Ur3)**	1190 m	**Ur3**	1190 m (the complete profile)
	Overlap of 180 m (320–500 m of Ur2 profile was not analysed)			
	Urbión 2 (Ur2)	500 m	**Ur2**	320 m (from 0 to 320 m)
	Gap of 30 m (no profile)			
	Urbión 1 (Ur 1)	905 m	**Ur1**	905 m (the complete profile)
	Total:	6312 m	Total:	5860 m (6070 m included gaps)
	Magnetic surveyed following paths (additional logs for methodological purposes)			
Urbión Gr.	**Upper part (UrU)**	1052 m	**UrU**	1052 m (the complete profile)
	Lower part (UrL)	1930 m	**UrL**	1930 m (the complete profile)
Magnetic susceptibility survey				
Urbión Gr.	**UrS**	2769 m	**UrS**	2769 m (the complete profile)

The En3-Ol1 profile includes the upper part of the Enciso Group and the lowermost part of the Oliván Group (Fig. 3F). Each unit shows its distinct magnetic signatures in this profile: the Enciso Group (En3) is pinpointed by low-amplitude, high frequency anomalies, whereas the Oliván Group (Ol1) shows a lower frequency pattern. This trend is also present in profiles Ol2 and Ol3 (Fig. 3G,H). Nevertheless, some differences can also be observed between the lower part of the Oliván Group and its upper part, where, in general, amplitudes and wavelengths increase. This is especially evident in the Ol2 profile. All in all, the Oliván Group can be characterized by three different segments: an initial one (Ol2; 0–500 m) with low-amplitude anomalies, a second segment (upper part of Ol2 and lower part of Ol3) with anomalies on the range of 10 nT in amplitude and an average wavelength of 30–40 m, and a final segment (upper Ol3, 450 m thick) with low-amplitude anomalies. The second and the third segments are separated by a 110 m-thick gap due to the magnetic noise of two wind turbines (Fig. 3H, I).

4.1.2. Magnetic survey following unpaved roads

The UrL and UrU profiles were surveyed following forest roads and paths (Fig. S3). The results (Fig. 4A) are similar to their regular equivalent profiles (UR1 to Ur3). UrL is characterized (i) by an average value of 10 nT of the total magnetic field anomaly, which decreases at the end of the profile, and (ii) by a series of peaks of short wavelength, and amplitude of ±10 nT, exceptionally ±30 nT. In the UrU profile, anomalies of up to 80 nT are recognized.

4.2. Magnetic susceptibility profile

The magnetic susceptibility of the Urbión Group, measured directly in the field (profile UrS; Fig. S3), shows an average of 117×10^{-6} SI, with extreme values of 339×10^{-6} SI and 4×10^{-6} SI, respectively (Fig. 4B). Despite the existence of some gaps, a trend with certain maxima (see running average of 12 data) can be defined. The magnetic susceptibility obtained from the laboratory samples shows a mean value of 240×10^{-6} SI, with a maximum of 449×10^{-6} SI and a minimum of 2.2×10^{-6} SI. The correlation between field and laboratory values fits a potential equation ($y = 1.0855x^{0.9279}$), with a Pearson's correlation coefficient of 0.96, indicating a remarkable covariation between the two data sets.

4.3. Cyclostratigraphy

4.3.1. Analysis of the merged profiles

The stratigraphic series analysed by cyclostratigraphy totals 5860 m (Table 1) that represent 96.5% of the stratigraphic succession (6070 m). The spectral analysis of the time series (see Fig. 3I) defines a cyclicity with important variations in its frequency, especially in the Urbión group, where cycles with different frequencies are present (Fig. 5A).

In the merged profiles, the Multi-Taper analysis of the complete time series (Fig. 6) show several peaks which surpass the 99% confidence level: 57.6, 80.5, 90.0 and 114.6 m, that correspond to those identified in the Fast Fourier Transform (FFT) spectrogram (Fig. 5B). All these values are referable to the long eccentricity cycle (E; 405 kyr). Other cycles appearing around 20 m, with main peaks at 21.4 m and 20.8 m, can be ascribed to short eccentricity (e; 100 kyr) cycles.

4.3.2. Urbión Group

The Multi-Taper analysis of the total magnetic field in the Urbión Group (2415 m out of the 2445 m thickness calculated for this group in the Cidacos section) was carried out gathering the Ur1, Ur2 and Ur3 profiles. Five peaks surpass the 99% confidence level (111.1 m, 58.8 m, 32.2 m, 21.7 m, and 20.8 m) and another peak (43.5 m) approaches this value (Fig. 7B). Their distribution along the stratigraphic series is, however, uneven (Fig. 7C). The 111.1 m cycle appears in most part of the series, but the 58.8 m cycle usually occurs where the former is not developed. The cycles of 32.2 m and 21.7–20.8 m appear more discontinuously, especially at the top of the Urbión Group. The spectral analysis of this interval (upper

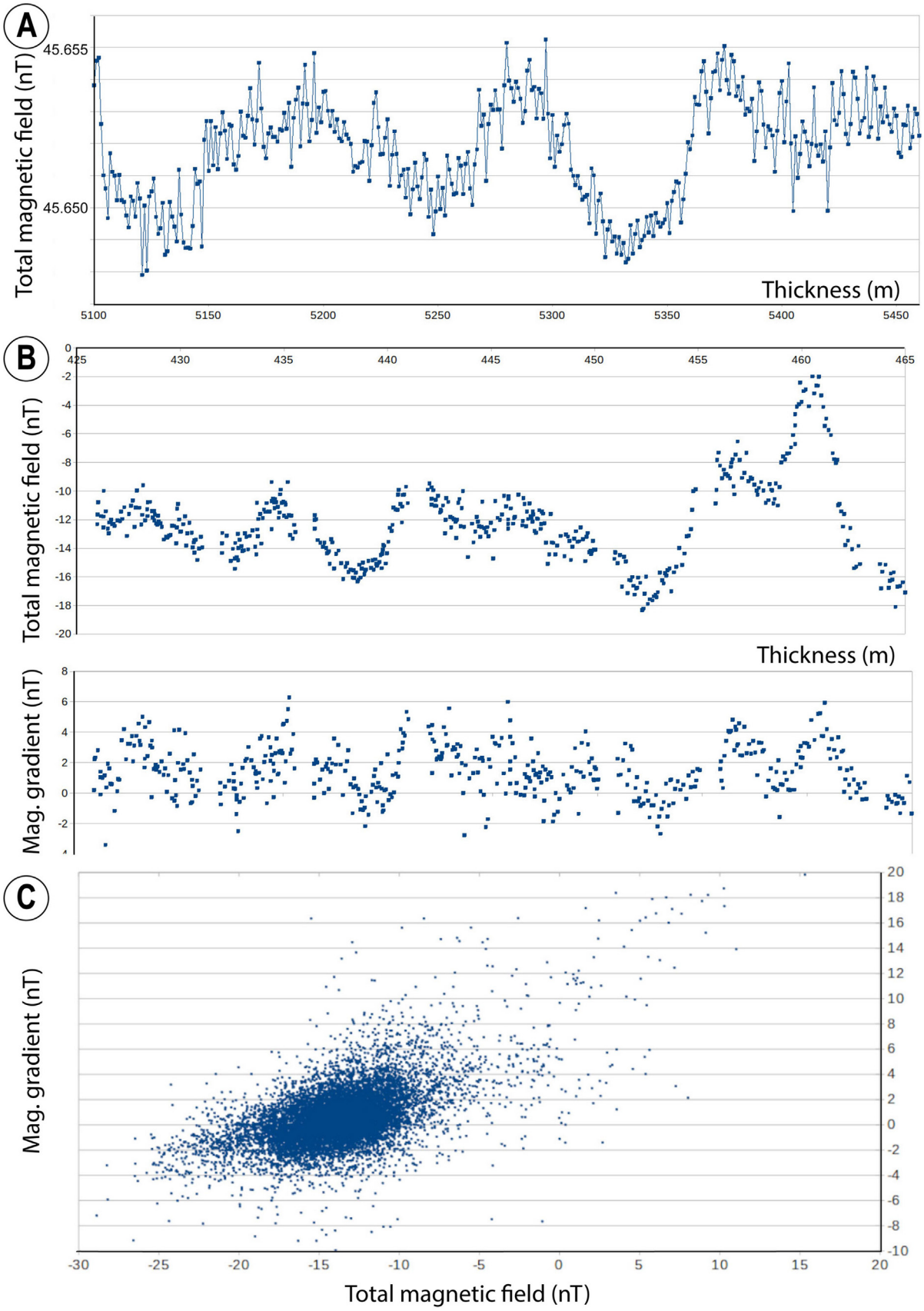

Fig. 2. (A) Raw data of the magnetic survey (part of Oliván 2 log), showing the actual accuracy of the survey. (B) Comparison between the data obtained from the total magnetic field (after the diurnal correction, upper diagram) and the gradient (lower diagram) in a part of the Ur1 log. Note the higher noise in the case of the gradient. (C) Correlation between the total magnetic field and the gradient for the whole of the dataset.

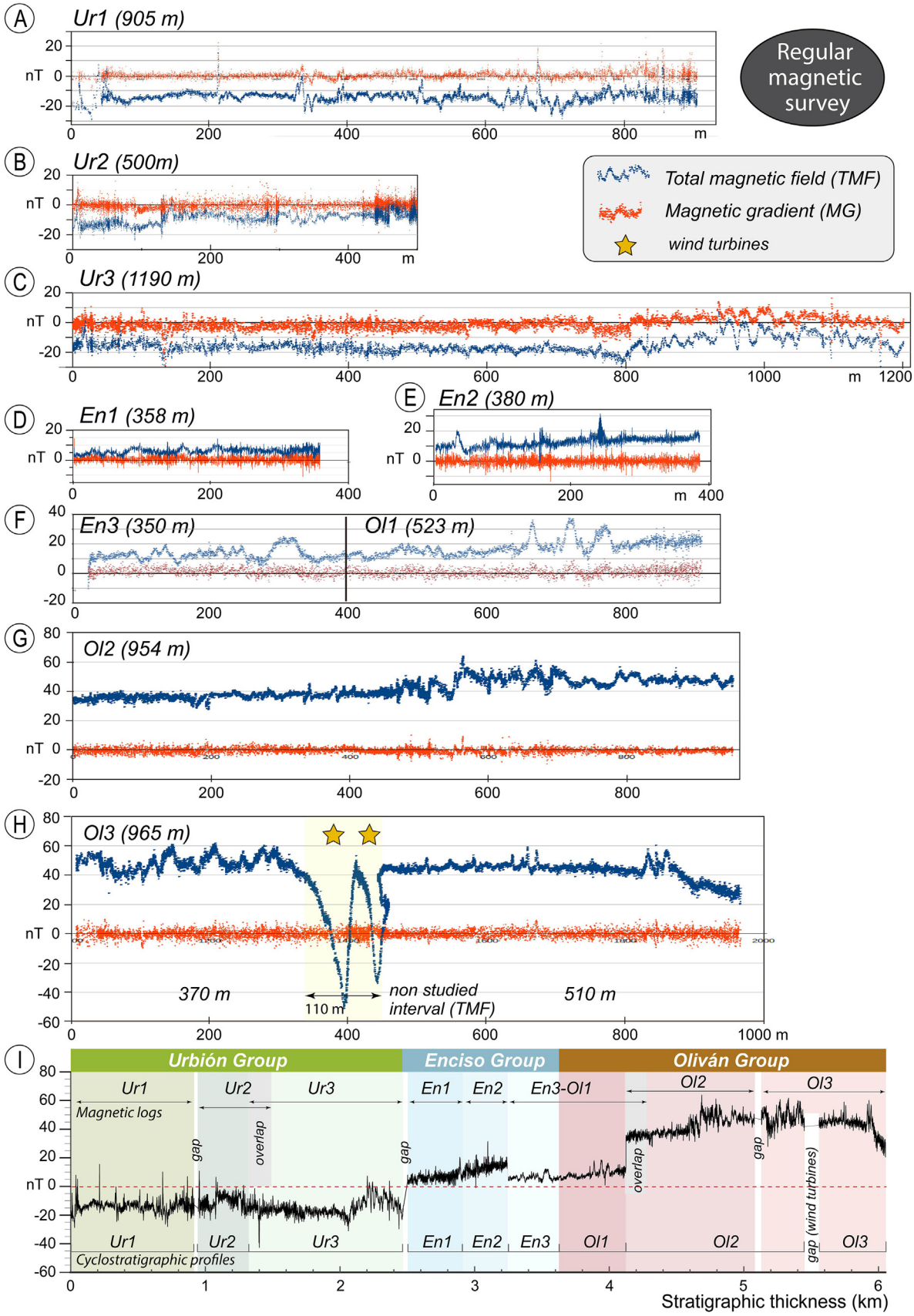

Fig. 3. Magnetic profiles (total magnetic field after diurnal correction and gradient) in the Urbión, Enciso and Oliván groups following a regular way of data acquisition (normal to bedding and taking advantage of scarp slopes) (Liesa et al., 2023). A) Ur1; B) Ur2; C) Ur3; D) En1; E) En2; F) En3-Ol1; G) Ol2; H) Ol3; I) Time series of the total magnetic field (after diurnal correction) built from the eight partial profiles (a to h), and partial cyclostratigraphic profiles for detailed analysis. Note the removed data associated with the wind turbines, which introduce a gap of 110 m between Ol2 and Ol3 cyclostratigraphic profiles.

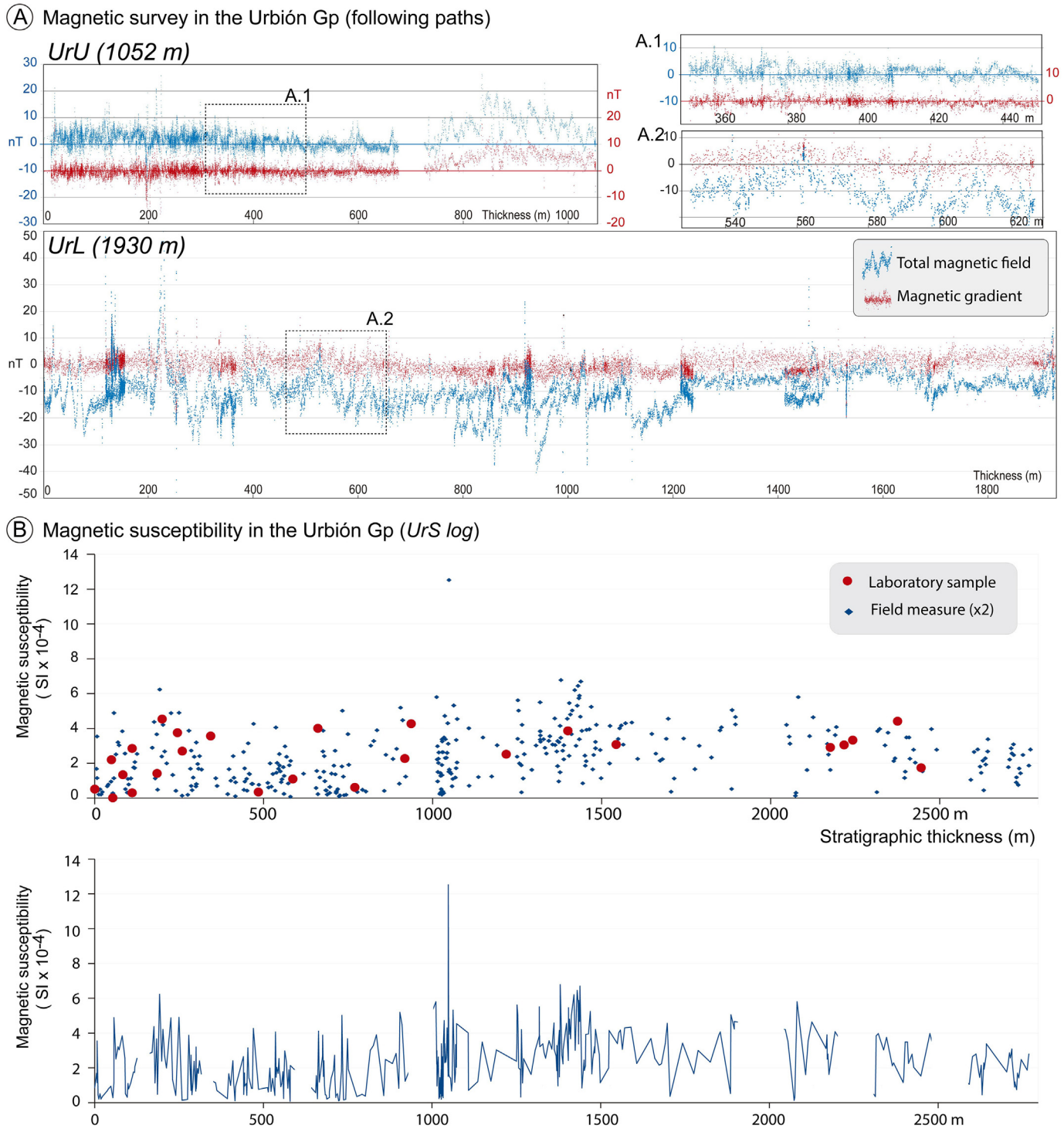

Fig. 4. (A) Magnetic survey in the Urbión Group following paths (UrL and UrU logs). Note that the total magnetic field (blue dots) and the magnetic gradient (red dots) data in UrU have been shifted vertically to avoid overlaps. (B) Magnetic susceptibility profiles in the Urbión Group (UrS log). Small blue points correspond to averaged data taken in the field, orange points correspond to laboratory measurements. The lower diagram is the curve joining the field data in order to enhance the cyclicity.

300 m) shows two cycles that exceed the 99% confidence level: 30.8 m and 20.1 m (Fig. 7D).

The results of the spectral analysis of the time series of the magnetic gradient and the total magnetic field acquired in the survey along unpaved forest roads (Fig. 8) are very similar. The same peaks, at 108–96 m and 41–33 m, surpass the 99% confidence level in the lower part (UrL profile), while in the upper part (UrU profile) higher frequency cycles (peaks at 39–40 m and 14–15 m) are better developed.

Similarly, the analysis of the time series corresponding to the discrete measurements of the magnetic susceptibility shows two frequency bands that surpass the 99.9% confidence level (Fig. 9). These frequency bands are at 67–170 m, with a main peak at 67.4 m, and 27–37 m. In this case, the higher frequency cyclicity is

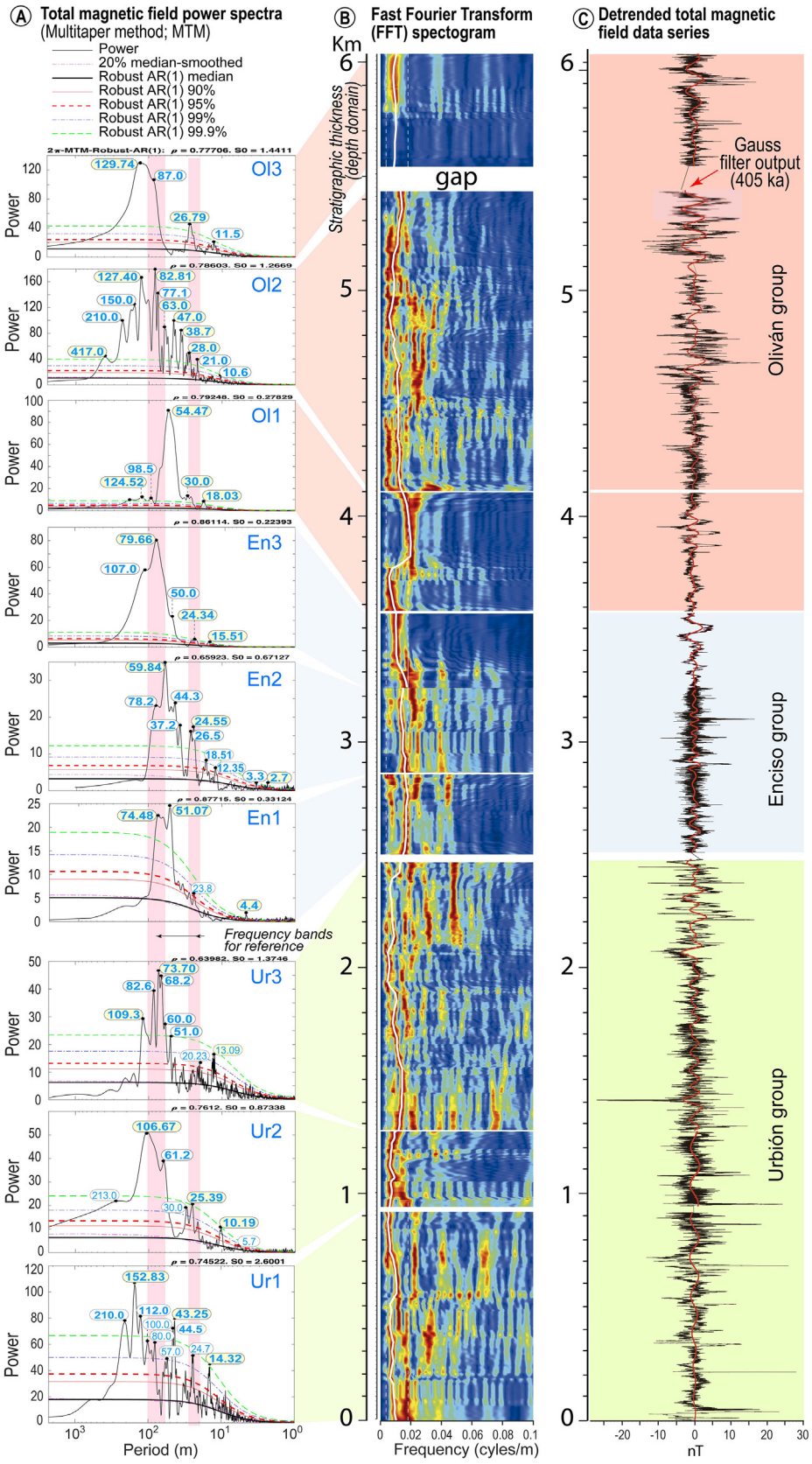

Fig. 5. (A) Multi-taper method power spectra of the nine partial time series of the total magnetic field (after diurnal correction) showing multiple cycles surpassing the 99% confidence band with certain continuity (and differences) between the different time series (pink frequency bands for comparison). (B) Evolutionary Fast Fourier Transform (FFT) spectrogram of these partial time series. The long eccentricity cycle (white line) with important variations in its frequency, conditioned by changes in sedimentation rates, is identified. The broken white vertical lines indicate the interval assigned by other authors to this cycle in the Enciso Group. (C) The complete time series detrended (black line) and filtered (red line) with a Gaussian filter with variable values throughout the series depending on the period of the long eccentricity cycle (405 kyr).

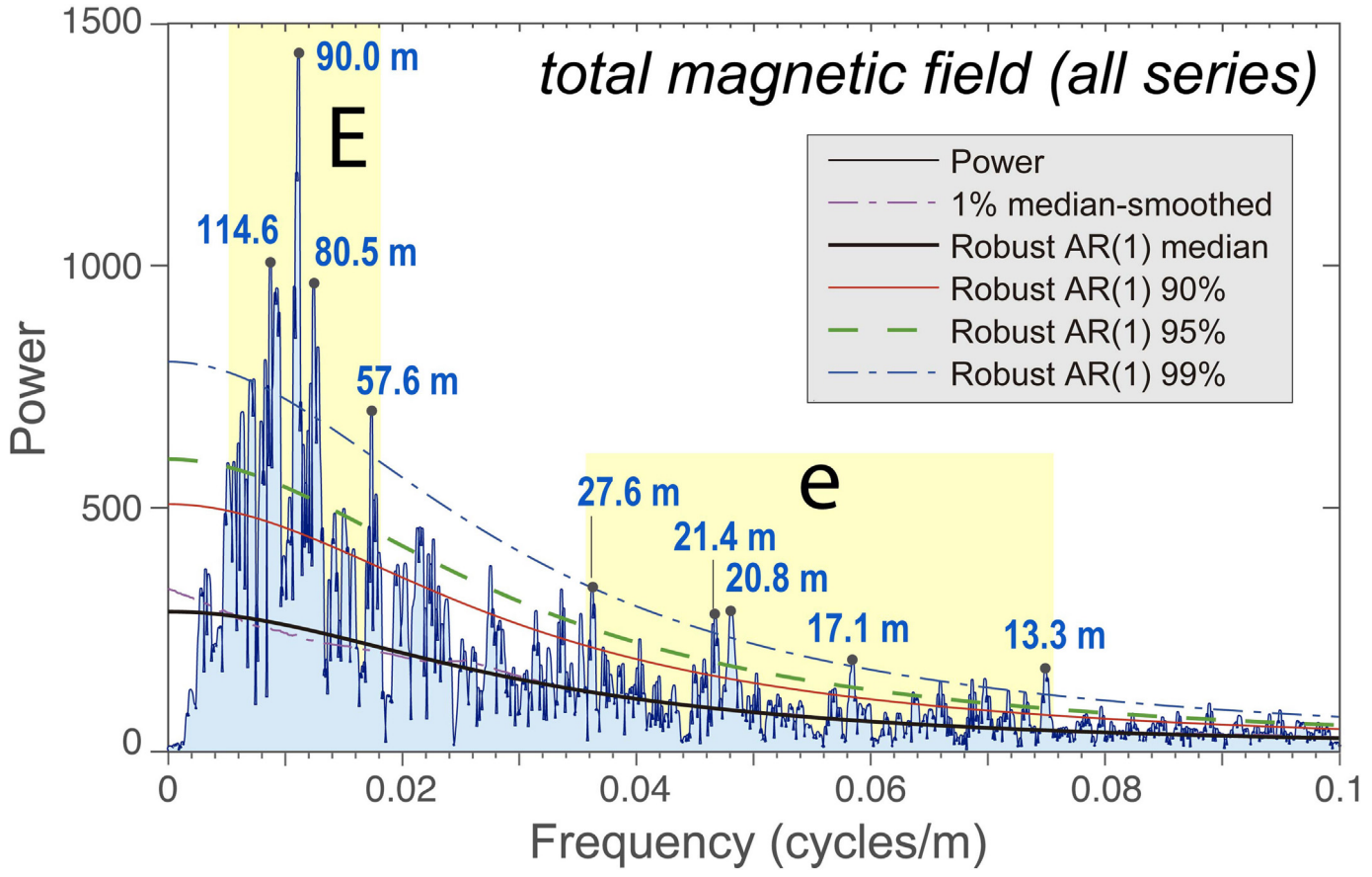

Fig. 6. Multi-Taper spectral analysis of the complete time series of the total magnetic field. A value of 2π MTM and a smoothing window of 1% were used.

not so well defined, possibly due to the higher spacing between measurements.

4.3.3. Enciso Group

The Multi-Taper analysis of the total magnetic field in the Enciso Group (1088 m out of 1108 m) was carried out gathering the En1, En2 and En3 profiles. The result shows two frequency bands surpassing the 99% confidence level (labelled as E and e in Fig. 10B). The first frequency band ranges from ~111 m to ~53 m (0.009 and 0.019 cycles/m, respectively), with two main peaks at ~88.9 m and ~57.9 m, respectively. The second one is narrower, with a main cycle in ~26.0 m. The distribution of the E frequency band along the stratigraphic series is particularly homogeneous (Fig. 10C), but it shows, however, a continuous variation in its trend, with the cycles of 57.9 m and 88.9 m developed mainly in the lower and upper middle part, respectively, with a gradual transition around 500–600 m.

4.3.4. Oliván Group

The Multi-Taper analysis of the total magnetic field of the Oliván Group (2353 m out of the 2517 m inferred in the Cidacos section) was carried out gathering the Ol1, Ol2 and Ol3 profiles. Seven peaks surpass the 99% confidence level (Fig. 11B). Four of them show very close frequency values (~154.8 m, ~112.9 m, ~88.8 m and ~82.1 m; E band) and continuous transitions (white line, Fig. 11C). The other three peaks have periodicities between 26.1 m and 46.7 m (e band), with a main cycle in ~37.0 m. These higher frequency cycles appear mainly in the central part of the stratigraphic series (metres 900–1500) (Fig. 11B,C).

The upper part of the Oliván Group (Ol2 and Ol3 merged profiles) shows two frequency bands surpassing the 99.9% confidence level (Fig. 11D). The first one has a maximum in the 517.4 m periodicity, but with a wide range (from 700 to 350 m). The second one has two neighbouring maxima in the periodicities, 105.0 m and 98.3 m.

5. Interpretation

5.1. Modelling and meaning of magnetic anomalies

The magnetic anomalies obtained can be directly related to the magnetic susceptibility of rocks, as checked in the field by direct measurements. In spite of this direct correlation, a non-negligible contribution of magnetic remanence (not recorded in the hand-held or laboratory susceptometer measurements) can also exist. Forward modelling in 2.5D has allowed us to determine the influence of (i) the magnetic properties, (ii) the different parameters related to the stratigraphic series and (iii) its outcrop conditions (Figs. 12 and 13). These parameters are the following:

Topography. It is interesting to note that the optimal scenario for creating well-defined anomalies is that of scarp slopes (i.e. slopes dipping opposite to the dip of beds), oriented to the South (in the case of the Cameros Basin, where bedding dips to the North dominate, Figs. S1, 12 and 13). Upon a flat topography, the vertical superposition of shallowly-dipping bodies would be lower (that is, a vertical borehole would cut a lower number of strata) than in the case of a scarp slope. However, if we consider the height of the sensor, the differences in distance (the shortest distance from the sensor to the ground) from the sensor to the different bodies are lower in the case of scarp slopes.

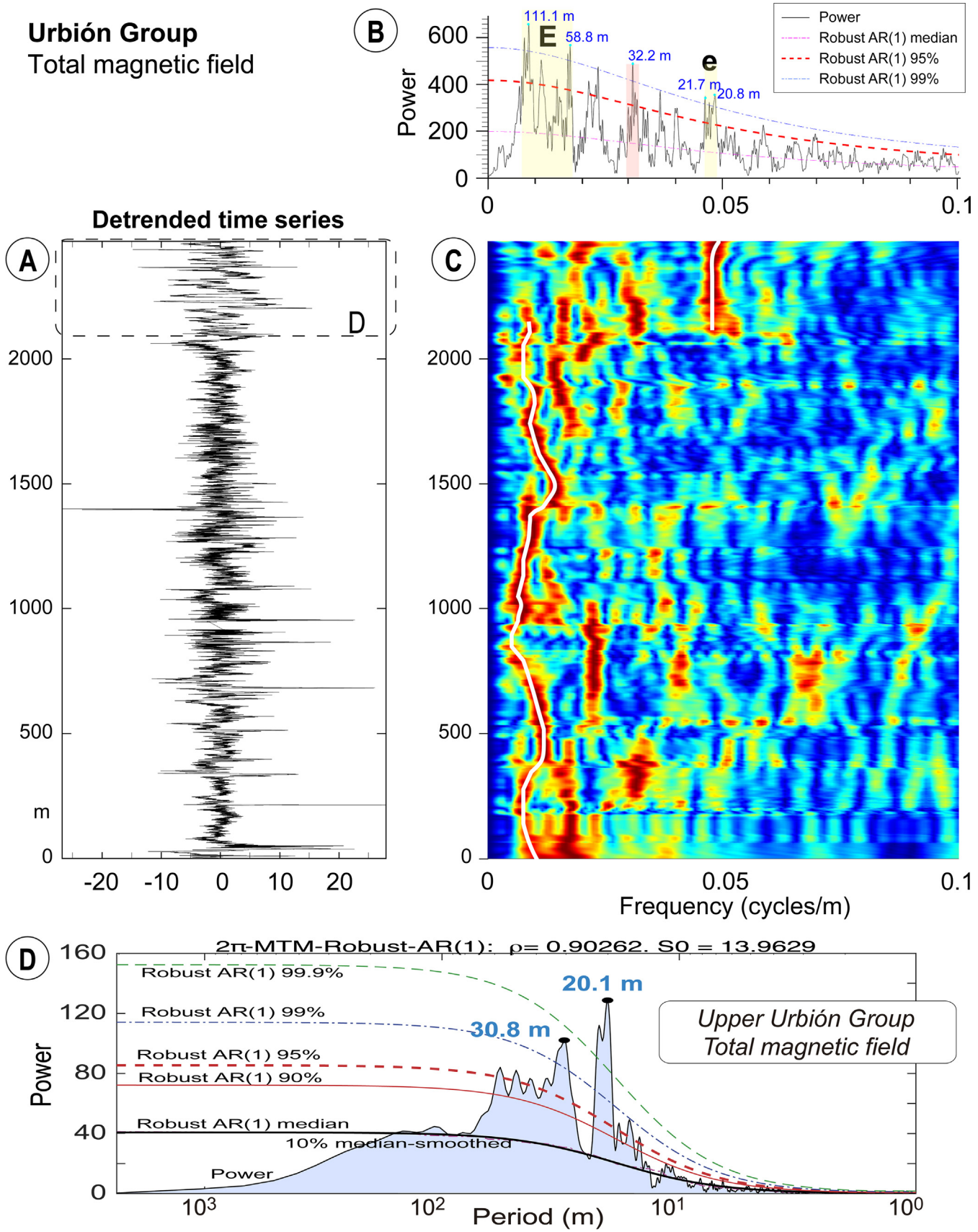

Fig. 7. Spectral analysis of the total magnetic field log (horizontal scale in nT) of the Urbión Group. (A) Detrended time series. (B) 2π MTM power spectrum (smoothing window of 1%). (C) Evolutionary FFT spectrogram of total magnetic field stratigraphic series with a 300 m sliding window. (D) 2π MTM power spectrum of the total magnetic field log of the upper part of the Urbión Group (smoothing window of 10%) showing two well-defined cycles exceeding the 99% confidence band, referable to the 100-kyr eccentricity cycle.

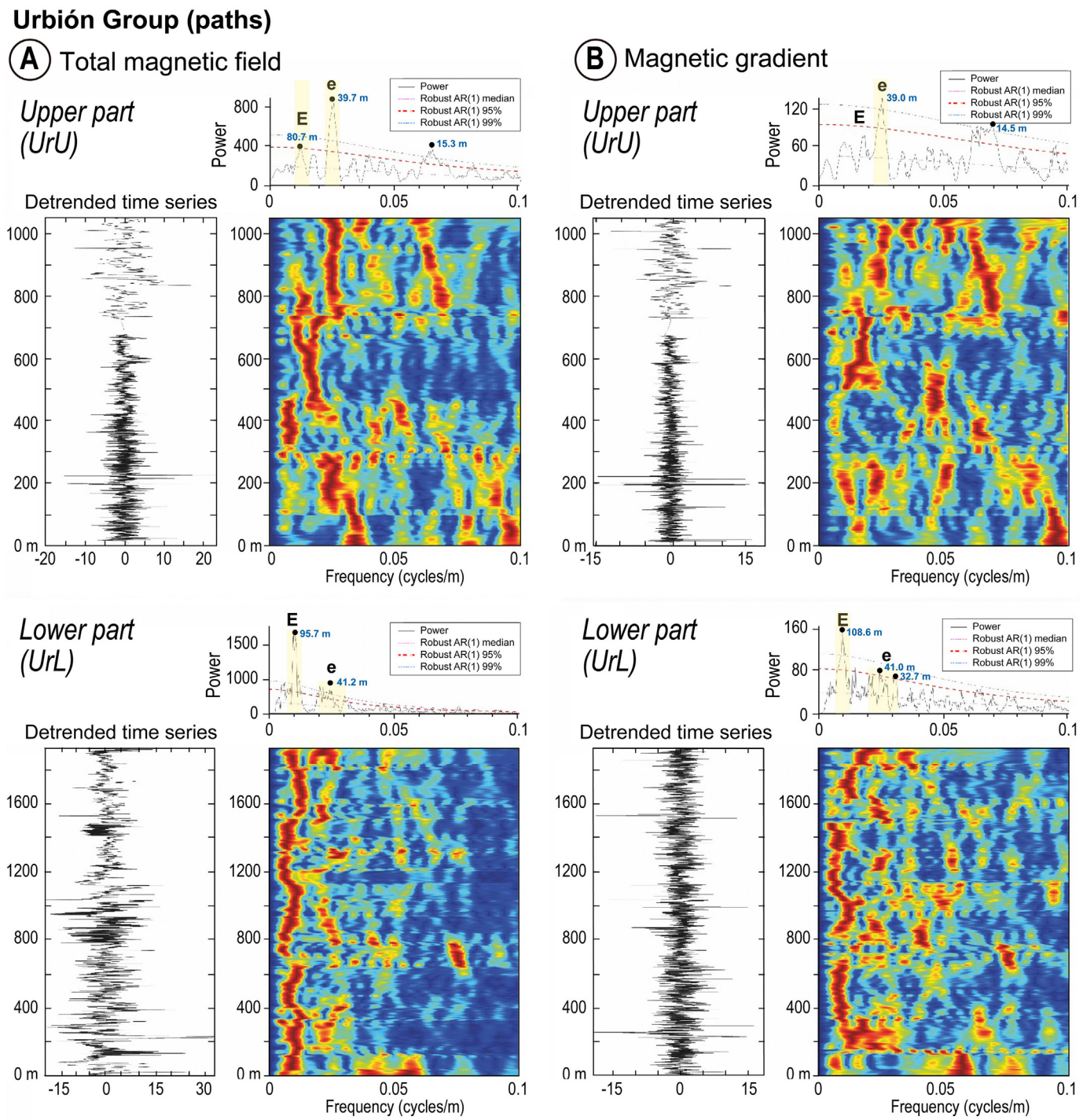

Fig. 8. Spectral analysis (MTM and Evolutionary Spectral Analysis) of the time series of (A) total magnetic field and (B) magnetic gradient of the lower and upper parts of the Urbión Group measured along forest roads (UrL and UrU profiles, respectively). Horizontal scale of detrended time series in nT. The trend has been eliminated by means of a LOWESS model (Cleveland, 1981) and a window of 200 m has been used. Two frequency bands (E and e), corresponding to the two frequencies of the eccentricity cycle (long and short eccentricity, respectively), appear well defined.

Contrast of magnetic properties (Fig. 12A). Under conditions of homogeneous magnetic remanence, the values of the magnetic anomaly (2–4 nT in amplitude for each individual anomaly and wavelengths of one to several metres) can be explained by changes in the magnetic susceptibility of about 400 $\times$ 10^{-6} SI. However, susceptibility changes of 200 $\times$ 10^{-6} SI would guarantee magnetic anomalies within the measurable range. When contrasts of susceptibility are lower than 200 $\times$ 10^{-6} SI, differences in the intensity of the remanence (between 10 and 50 mA/m) must be considered if significant magnetic anomalies have been obtained. If the two parameters, magnetic susceptibility and remanence, change between different stratigraphic units, which is probable because both of them depend on the iron and ferromagnetic minerals content and are often correlated (Dietze et al., 2011;

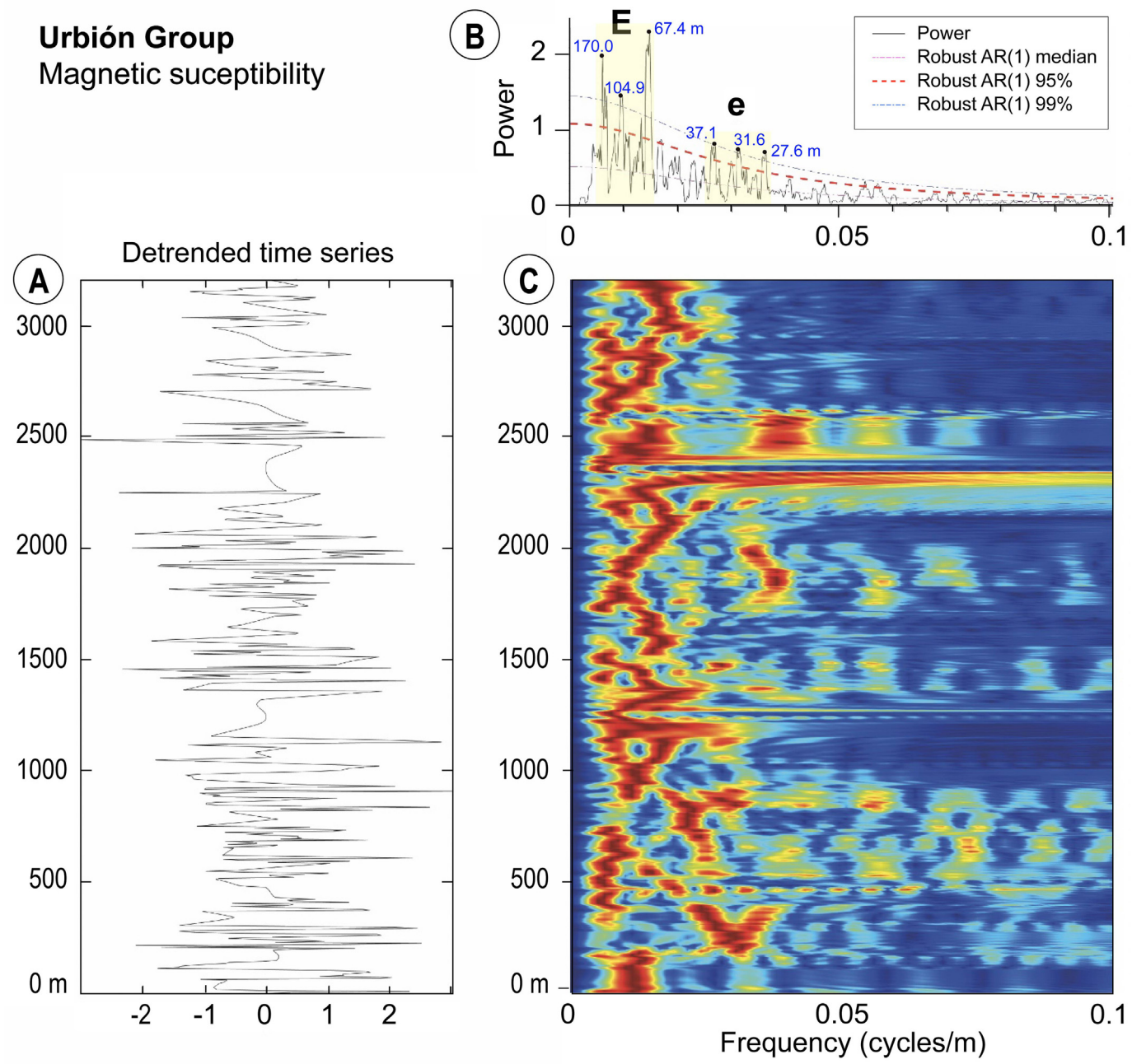

Fig. 9. The spectral analysis (Evolutionary Spectral Analysis) of the time series of the discrete measurements of magnetic susceptibility in the Urbión Group shows two poorly defined band that can be referred to the long (E) and short (e) eccentricity cycles, respectively. The trend has been eliminated by means of a LOWESS model (Cleveland, 1981) and a 200 m window.

Singsoupho et al., 2015; Dentith et al., 2020), the magnetic anomalies can reach greater amplitudes.

The dip of the geological body, combined with the orientation of the profile, is a major issue influencing the shape (wavelength and amplitude) of the magnetic anomalies (see, e.g. Hinze et al., 2013). When the strata show a northwards dip that approaches the inclination of the Earth's magnetic field, and the dip direction is opposite to the inclination of the slope (scarp slope), the anomalies generated are almost symmetrical. This enhances the anomaly pattern and simplifies its subsequent analysis (Fig. 13). This happens, in our case, in spite of being located at latitudes of 42° in the northern hemisphere, where the inclination of the magnetic field is 56° N (and therefore magnetic anomalies are typically asymmetric and dipolar). This situation is in contrast with hypothetical anomalies generated by beds dipping to the South at this latitude, which would show a strong asymmetry, especially when the topography is not flat. For profiles that have an E–W direction (i.e. transects of stratigraphic series approaching a N–S strike), there would also be a good definition and symmetry of magnetic anomalies, provided that there are contrasts of magnetic properties between the different bodies.

Depth to the causative body (Fig. 13B, C). The short wavelengths of the magnetic anomalies obtained in the magnetic profiles indicate a shallow depth of the causative bodies (Fig. 13B). In fact, only the shallower 5–10 m in the subsoil have a direct influence in short-wavelength anomalies, because the influence of magnetic

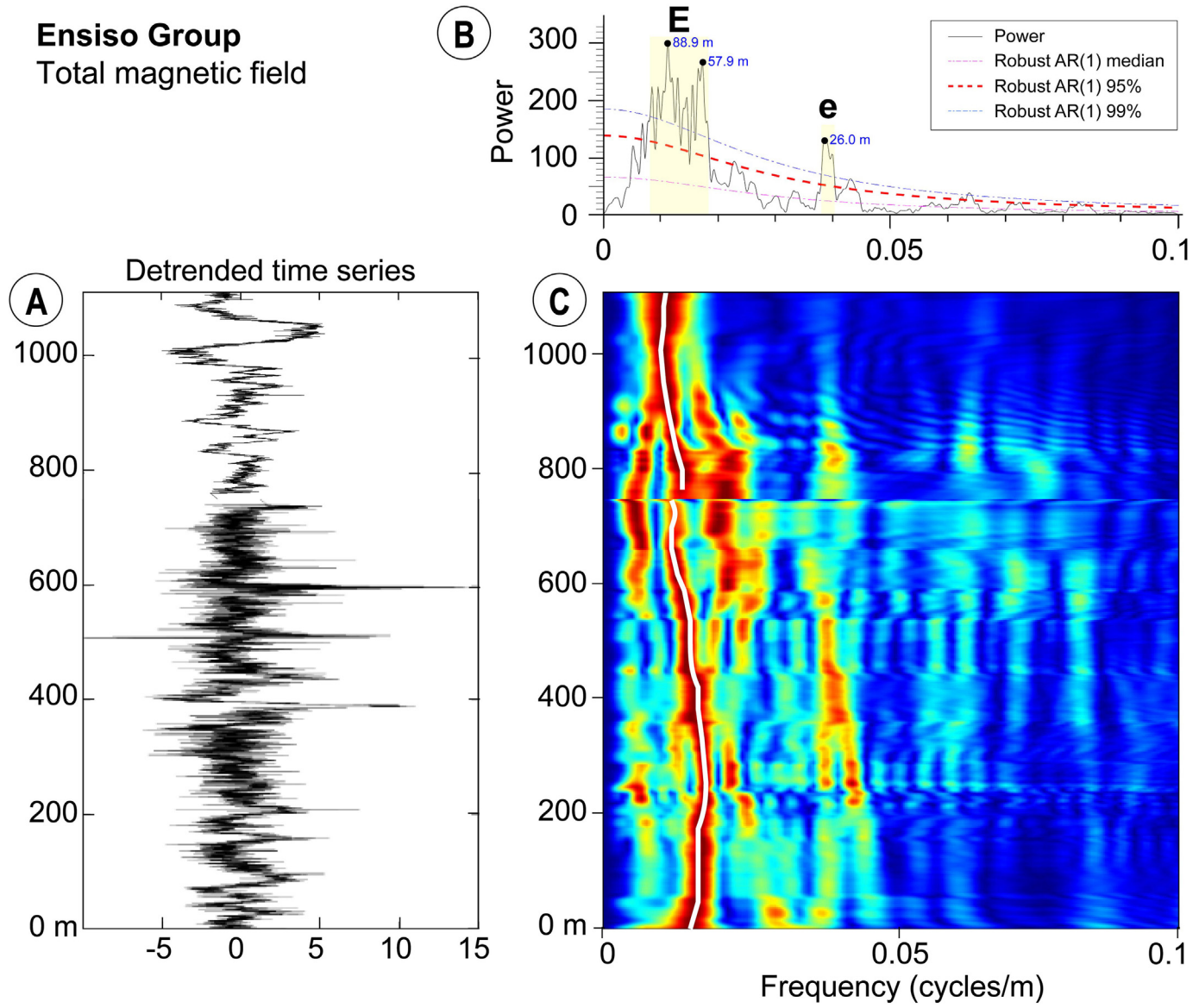

Fig. 10. Spectral analysis of the total magnetic field stratigraphic series of the Enciso Group. (A) Detrended time series. (B) 2π MTM power spectrum (smoothing window of 1%). C) Evolutionary FFT spectrogram of the total magnetic field stratigraphic series with a 200 m sliding window.

properties strongly diminishes as depth to the causative body increases. A different scenario appears when the causative body is buried below a non-magnetic cover or a soil (that can be magnetic or non-magnetic). When the thickness of the latter is greater than 1 m, the influence of the target body (for normal values of susceptibility) in the magnetic field measured at surface (for short-wavelength anomalies) is negligible (Fig. 13C, central body, magnetic anomaly indicated by the dotted line). This factor can therefore limit the applicability of the technique. In the studied case, soils are scarcely developed (a few centimetres thick in average). However, since processes linked to soil formation and evolution (including wildfires) can be responsible for the formation of magnetite, areas with good development of organic and topsoil horizons should be avoided.

The features of the sedimentary sequence. The influence of adjacent beds also limits the possible individualisation of magnetic anomalies linked to particular units (Fig. 13A). The presence of strata with distinct magnetic properties favours the interpretation of the magnetic anomalies in terms of magnetic susceptibility. Because of the stronger influence of surficial zones and the weaker influence of deeper units (as we have shown in the previous points), the vertical superposition of different bodies does not necessarily mean that their magnetic signals will interfere. Along the horizontal line, a separation between causative bodies equivalent to (at least) their thickness (4 m in the example presented) guarantees the individualization of the anomalies associated to each one of them.

All the above-described factors influence both the anomalies of the total magnetic field and the magnetic gradient. The short-wavelength, low-amplitude magnetic anomalies obtained (several nT in amplitude with wavelengths of a few metres or less) can be interpreted considering magnetic susceptibilities ranging from 0 or negative in the quartzitic layers to ca. 400×10^{-6} SI in pelitic beds, and comparable values of magnetic remanence. These contrasts of susceptibility are found in the Urbión Group, where the thickness of layers is also the adequate for creating individualized, measurable magnetic anomalies. Oxydised pyrites (cubic crystals whose size varies from milimeters to centimetres) were observed in the

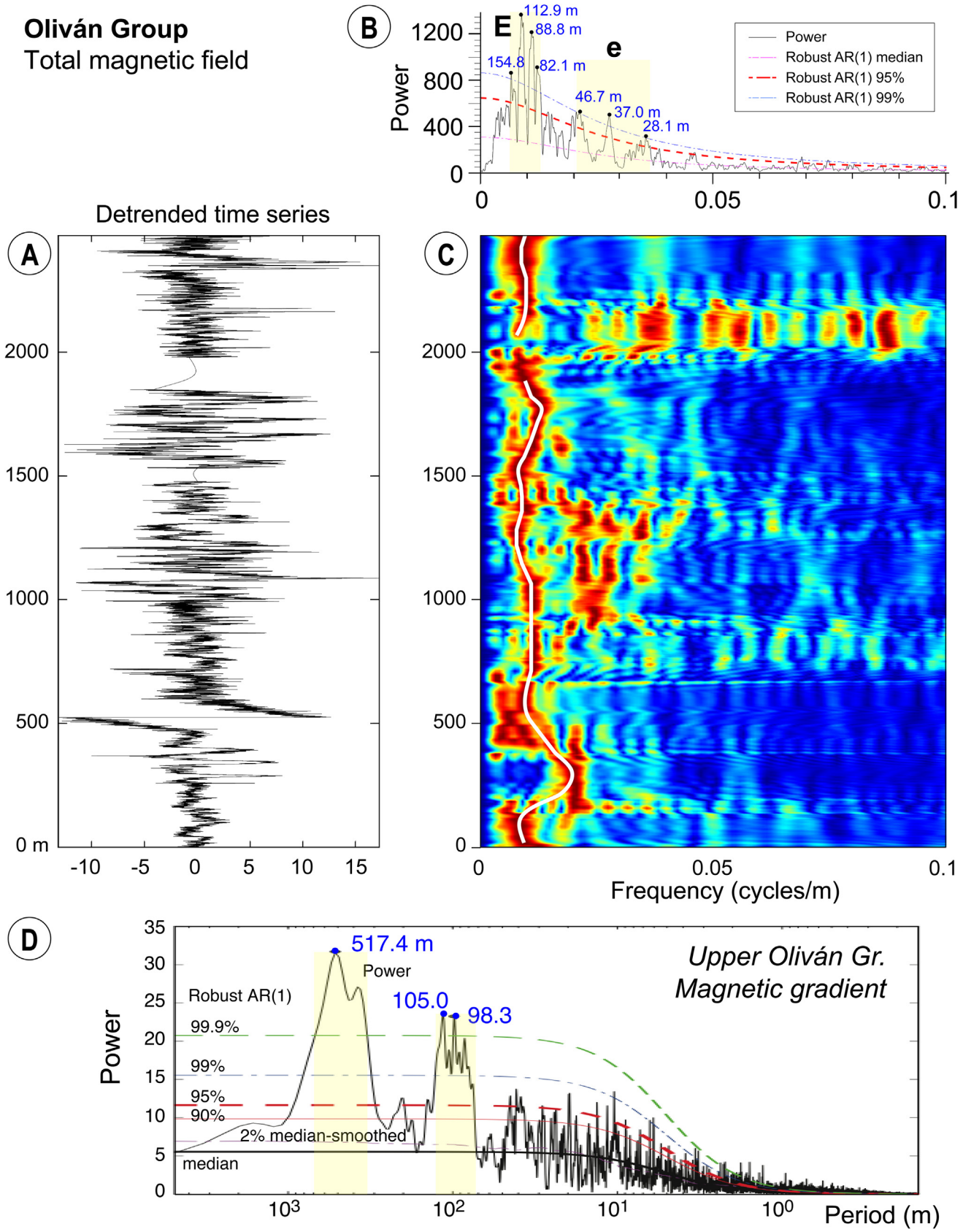

Fig. 11. (A), (B) and (C) spectral analysis of the total magnetic field stratigraphic series of the Oliván Group. (A) Detrended time series (horizontal scale in nT). (B) 2π MTM power spectrum (smoothing window of 1%). (C) Evolutionary FFT spectrogram of total magnetic field stratigraphic series with a 300 m sliding window. (D) Multi-Taper spectral analysis of the magnetic gradient time series of the upper part of Oliván Group (Ol2+Ol3 profiles), showing two very well-defined frequency bands (350–700 m and 65–105 m) that exceed the 99.9% confidence band (peaks of 98.3 m and 517.4 m), referable to the eccentricity cycles of 405 kyr and 2.4 myr, respectively. A value of 2π MTM and a smoothing window of 2% have been used.

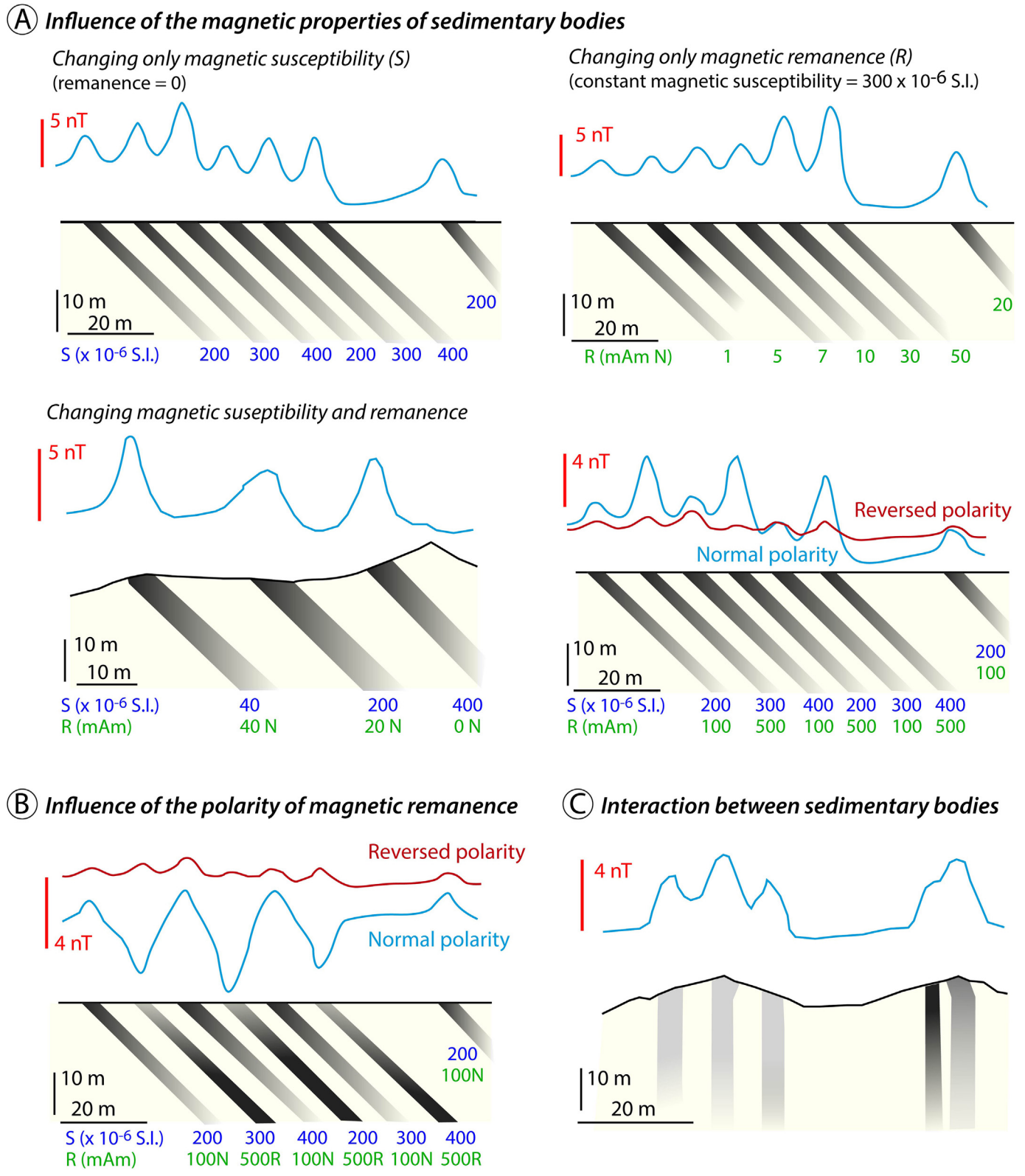

Fig. 12. Modelling of the different parameters (magnetic susceptibility and remanence) influencing the features of the magnetic anomalies. (A) Magnetic susceptibility and remanence of the sedimentary bodies. (B) The polarity of the magnetic remanence. (C) Interactions between sedimentary bodies. See text for explanation.

exposures, but direct measurements of susceptibility indicate that weathering does not have consequences in their magnetic susceptibility, which must rather correspond to of the global iron content of the rock. In the Enciso Group, magnetic susceptibility is more homogeneous, and stratigraphic layers with contrasting properties are thinner, resulting in smaller magnetic anomalies and more monotonous profiles, that, nevertheless, can also be interpreted in terms of cyclicity. In the Oliván Group, lithological

contrasts are not so strong as in the Urbión Group, but the thickness of units with contrasting properties is also of several metres. The upper part of this unit is pinpointed by differences that must be related to susceptibility changes. The magnetic signature of each of the studied units, and their different segments, is therefore present in the magnetic profiles.

5.2. Stratigraphic cycles

The cyclostratigraphic analysis shows consistent results for each individual profile, each sedimentary group, and the merged profile. Two main frequency bands (E and e) can be distinguished (Table 2). The occurrence of close maxima within the E frequency band and their successive positions along the stratigraphic series (relaying along the stratigraphic logs, Figs. 7, 10 and 11) are interpreted to represent the same cycle. The significant variations in the cycle frequency could be conditioned by changes over time in the sedimentation rates (e.g., Angulo and Muñoz, 2013; Muñoz et al., 2020). The ascription of the E main cycle to the long eccentricity cycle (405 kyr) is based on previous results in the Enciso Group (Doublet, 2004; Angulo and Muñoz, 2013; Hernán, 2018; Muñoz et al., 2020) that show values between 68 and 131.8 m. In this work, the long eccentricity cycle normally varies between 55 and 115 m, with maxima up to 170 m. The highest values correspond to the detrital Urbión and Oliván groups, deposited in fluvial environments, whereas the lowest values were inferred in the Enciso Group, richer in carbonates and deposited in lacustrine to deltaic environments. The main e cycle (15–35 m) represents the short eccentricity cycle (100 kyr), according to its relation with the E cycle (ratio close to 4:1) in all the profiles (Table 2).

After applying a Gaussian filter, centred on the values identified for the long eccentricity cycle (405 kyr) in each profile, we infer 27 cycles in the Urbión Group (~11.2 Ma), 19 cycles in the Enciso Group (~7.7 Ma) and 29 cycles (~11.7 Ma) in the Oliván Group (Figs. 5C and 14). Accordingly, the studied stratigraphic series spans about ~30.6 myr (Fig. 14), with a mean sedimentation rate (without decompacting the deposits) of ~0.2 mm/yr (198 m/myr; 6070 m in 30.6 myr), and extreme values of 99 m/myr (middle part of the Enciso Group) and 360 m/myr (lower part of the Urbión Group). The sedimentation rate allows the definition of three main stages with values of 350 m/myr (cycles 1– 9), 146 m/myr (cycles 10–42), and 212 m/myr (cycles 43– 76). The Urbión, Enciso and Oliván groups have mean sedimentation rates of 222 m/myr, 144 m/myr, and 215 m/myr, respectively.

6. Discussion

6.1. Magnetic surveying as a proxy for cyclicity and palaeoclimatic studies

Magnetic surveying had not been used, until now, as a paleoclimate proxy. In this work, we show that short-wavelength magnetic anomalies respond precisely to the magnetic properties of rocks and show a cyclicity referable to Milankovitch's (1941) frequency band. The main magnetic proxy used in palaeoclimatic studies has been the direct measurement of magnetic susceptibility (e.g., Ellwood et al., 2000; Da Silva et al., 2013; Kodama and Hinnov, 2014; Oliva-Urcia et al., 2016; Liu et al., 2020; Pfeifer et al., 2020; Powers et al., 2020; Omar et al., 2021; Golovanova et al., 2023), but the results obtained in the Cameros Basin allow us to conclude that the values of the total magnetic field and the magnetic gradient can also be used to infer iron contents. Besides, the closest sample spacing made possible by this technique improves the discrete sampling method: in the eight studied profiles, the mean of the distances between measurements were 0.10 m, 0.19 m, 0.07 m, 0.16 m, 0.11 m, 0.17 m, 0.19 m and 0.20 m (modes show lower values in all cases), whereas the average distance between discrete susceptibility measurements was in this case 7.77 m. Furthermore, the measurement of the magnetic field and gradient, measured at a constant height, smooths the signal in the same way that an upward continuation, eliminating the noise derived from small surficial elements. The good outcrop conditions, continuity and thickness of the stratigraphic series, together with the favourable geometrical relationship between the structure (N-dipping monoclinal series of the SW limb of the Cameros syncline) and the topography (scarp slopes), contribute significantly to the quality of the magnetic signal and make easier its interpretation in terms of paleoclimate.

The advantages of using magnetometric surveys with respect to direct measurements of susceptibility are therefore:

1) The higher number of measurements, that for a normal velocity of acquisition (the average in this work was 1.5 km/h) can be as high as 1 measurement every 5–20 cm. For sedimentary sequences of thousands of metres, as the one studied in the Cameros Basin, this sampling frequency is beyond the reach of conventional, discrete susceptibility measurements.
2) The representativeness of the measurements taken, that in the case of magnetic surveys is higher, because an only measurement averages the susceptibility of a volume of several cubic metres of rock. In contrast, the individual measurement of a hand-held susceptometer or a laboratory measurement corresponds to tens of cubic centimetres of rock.
3) The magnetic survey allows for non-outcropping units to be represented in the magnetic log, thus avoiding possible gaps appearing when using the discrete measurements method (although gaps resulting from magnetic noise or geological faults can also appear).

The proposed technique opens a promising field for cyclostratigraphic analysis. Since magnetometer consoles allow the addition of labels to pinpoint the beginning and end of sedimentary units, and, besides, time is accurately recorded for each measurement, GPS accuracy is not a critical issue. This issue is especially important when walking along steep scarp slopes.

The limitations of magnetometry for defining sedimentary cycles are related to (i) the outcrop conditions and the presence of a soil cover, (ii) the ambient magnetic noise, (iii) the (absence of) contrast of susceptibility between different sedimentary bodies and (iv) the possible interference between magnetic susceptibility and magnetic remanence (if magnetic reversals are recorded). The anomaly in the total magnetic field created by a particular body depends on its distance to the sensor and its magnetic susceptibility relative to surrounding bodies. If the ratio of susceptibility between a bed and the underlying and overlying strata is between 2:1 and 10:1, it generates a distinct magnetic signal (reflected in a magnetic anomaly) that does not interfere with the signals from adjacent units. This is valid for strata whose thicknesses range between 0.5 m and 5 m (for sampling distances between 5 and 20 cm). The relationship between the dip of strata and the slopes is also an important issue. Because of the vertical configuration of the device (two sensors are used for the measurement of the gradient and the GPS antenna is on top of them) the optimal relationship is that of vertical strata below a flat surface, and the worst one would be horizontal strata cropping out on a steep slope. The intermediate geometries between these two end-members will show cleaner or noisier profiles, depending on the combination of the two factors. Configurations in which the slope and the sedimentary series show the same dip direction can be considered as unfavourable. This also applies when measuring a stratigraphic section (Fig. S2B). The

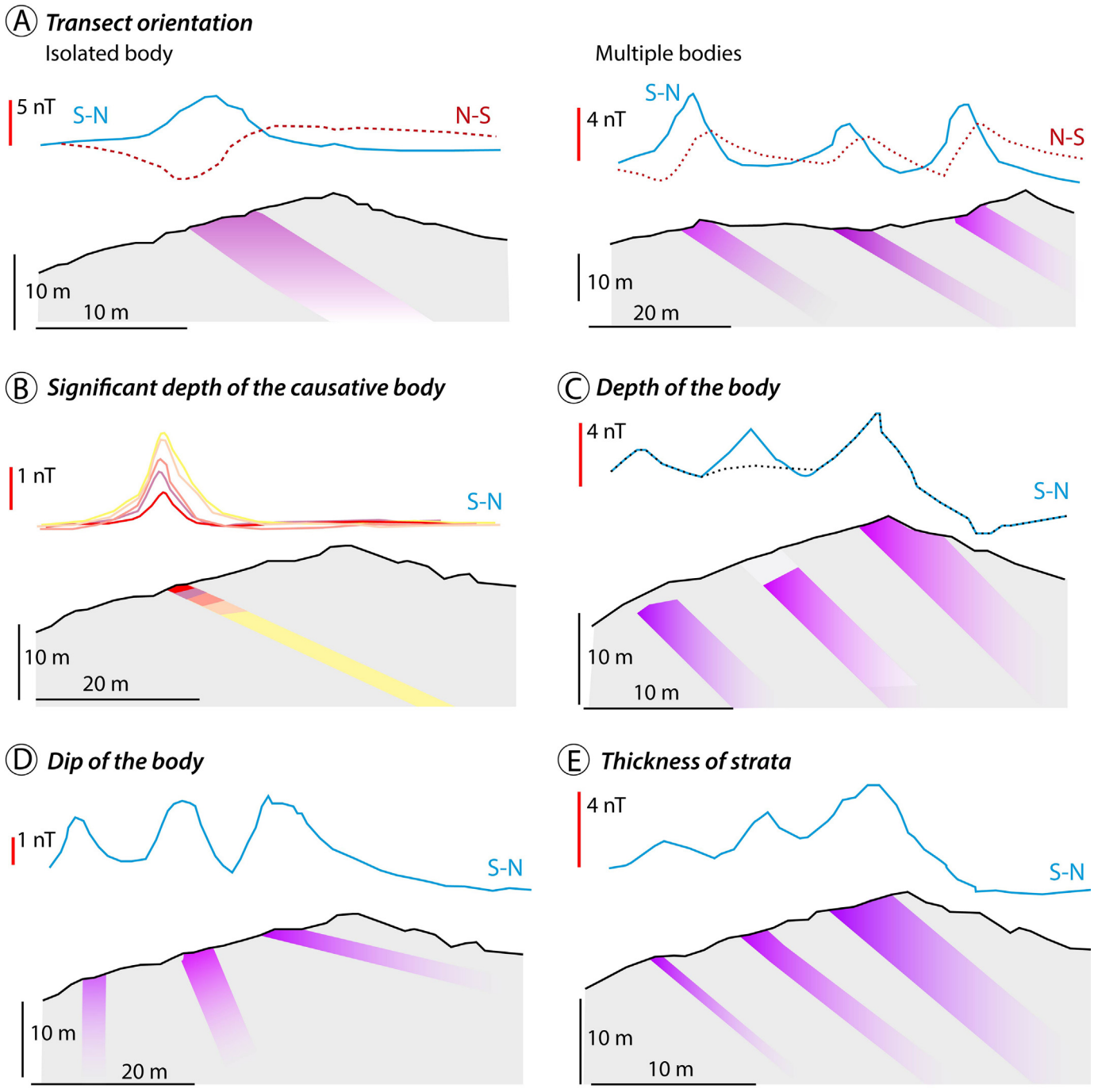

Fig. 13. Modelling of the different parameters such as (A) the orientation of transect, with series of different bodies vs. and isolated body, (B) the significant depth of the causative body, (D) the depth to the body, and (C) the dip of the sedimentary body and (E) the thickness of strata. See text for explanation.

magnetic remanence can influence the shape of magnetic anomalies, especially if the sedimentary sequence shows different remanence directions (i.e. when the main paleomagnetic component is primary and the series is not included within a superchron). In thick sedimentary sequences, the existence of remagnetizations involving the whole basin is relatively common (Villalaín et al., 2003; Soto et al., 2008; Torres-López et al., 2016), in which case the orientation of the remanence would be constant (provided that there is a fairly constant dip of the stratigraphic series). In this case, only its module can influence the magnetic anomalies, in a way similar to magnetic susceptibility. The relationship between the two properties is usually direct, and their contribution to the total magnetisation depends on the Koenigsberger ratio in different rock types (e.g. Collinson, 1967; Dentith et al., 2020). Since the analysis of cyclicity is based on changes rather than in the absolute values of the anomalies, we do not expect a negative influence of magnetic remanence in the results. Nevertheless, new data in areas in which reversals of the Earth's magnetic field are recorded in the remanent magnetisation, are needed to check the wider applicability of the proposed technique.

In this work we have also checked the influence of other variables, such as the walking velocity of the rover magnetometer and

Table 2
Peaks (period in metres) above 99% confidence level of magnetic survey power spectra processed in this study and their correspondence with predicted Milankovitch cycles for 152–100 Ma. TMF, total magnetic field; MG, magnetic gradient; MS, magnetic susceptibility. Normal and Paths refers, respectively, to the two different ways for data acquisition, that is, perpendicular to bedding along the scarp slopes (regular magnetic survey) or following non-paved roads or paths. In bold, main periodicities.

Overall section	Urbión Group				Enciso Group	Oliván Group		Milankovicth cycles		Predicted Milankovitch cycles for 152–100 Ma	
TMF (normal)	TMF (normal)	TMF (paths)	MG (paths)	MS (paths)	TMF (normal)	TMF (normal)	MG (normal)	Band	Ratio	Ratio	Period (kyr)
							517.4	Very long eccentricity	0.18	0.17	2400
				170.0		154.6		Mean 94.0	1	1	405
114.6	**111.1**		**108.6**	104.9		**112.9**	**105.0**	**E band** (long eccentricity)			
90.0		**96.7**			**88.9**	88.8	98.3				
80.5		80.7				82.1					
57.6	**58.8**			**67.4**	**57.9**	46.7					
27.6	32.2	41.2	41.0	37.1		**37.0**		Mean 27.8	3.38	4.05–3.24	100–125
21.4	21.7	**39.7**	**39.0**	31.6		28.1		**e band** (short eccentricity)			
20.8	**20.8**		32.7	**27.6**	**26.0**						
17.1		**15.3**	**14.5**								
13.3											

the survey direction (uphill/downdip or downhill/updip on scarp slopes). None of these variables seems to be significant, provided that the surveyor walks slowly (about 1.5 km/h) and smoothly, without tilting the sensors during the survey. The orientation of the survey transects can influence the shape of the anomalies, especially when changing from a N–S to an E–W direction (assuming that both are perpendicular to the strike of bedding). However, sedimentary strata are planar features that extend along strike more than 1000 times their thickness across strike, what minimises this effect.

Another interesting possibility that we have explored is the survey along more accessible routes, taking advantage of unpaved forest roads (and avoiding as much as possible the sources of magnetic noise), instead of the more direct and secure option chosen in this work, that is, cross-country walking, perpendicular to the strike of bedding, along the scarp slopes. In the case of following unpaved forest roads, the control of faults is not so precise, and changes of orientation of beds must be carefully checked in each segment of the path. The UrL profile, surveyed in this way, is not directly comparable segment-to-segment with the equivalent profiles, because of lateral facies changes, but the global results in terms of cyclicity are similar. This opens the possibility to more flexible magnetic survey planning.

6.2. Chronostratigraphic implications

The Cameros Basin is the most important Cretaceous intra-plate basin in the Iberian Peninsula, with an 8 km-thick sedimentary filling deposited between the Tithonian and the Albian (Muñoz-Jiménez et al., 1997; Martín-Chivelet et al., 2019). In spite of this, the chronostratigraphic constraints are not very good and there are uncertainties about the age range of the series. This is due to several factors, namely (i) the continental character of most part of the syn-rift sequence, that contains an astonishing quantity of dinosaur tracks and bones but very few remains with biostratigraphic significance, (ii) the metamorphism experienced by the basin at the end of the rifting stage, that altered the organic-rich levels susceptible of containing pollen, (iii) the widespread remagnetization involving the whole basin, and the difficulties for finding a primary magnetic component, what precludes magnetostratigraphic analysis. In addition to this, there have been contradictory dating by means of charophytes and ostracods (the most frequent microfossils in the series) for the past 40 years. The main works using ostracods were done by (i) Kneuper-Haack (1966), who attributed the upper part of the Oliván Group to the Hauterivian, (ii) Salomon (1982), who assigned the Enciso Group to the Valanginian, and (iii) Schudack and Schudack (2009, 2011). In this latter work, the age of the Urbión Group was established as Late Berriasian and the Enciso Group as Late Valanginian–Barremian. Chronostratigraphic studies based on charophytes give in general younger ages: (i) Brenner (1976) considered that the age of the Oliván Group (top of the syn-rift series) is Aptian, (ii) Schudack (1987) assigned an Aptian age to the Enciso Group, thus considering that the Oliván Group would be Aptian–Albian and (iii) Martín-Closas (1989, 2000) and Martín-Closas and Alonso Millán (1998), mainly based on data from the western sector of the Cameros basin, considered that the whole of the syn-rift sequence is comprised between the Late Kimmeridgian and the Albian. Marine microfossils in the post-rift sequence (Muñoz-Jiménez et al., 1997) indicate an Albian–Cenomanian age for the end of the syn-rift sedimentation. More recent works (Moreno-Azanza et al., 2020) based on ootaxa have re-considered the age of the Enciso Group as Valanginian–Hauterivian. However, it must be taken into account that the correlation of the lower units of the basin has also been a matter of controversy (Casas et al., 2009).

According to the cyclicity analysis, a dating of the filling of the Cameros Basin from the Urbión Group upwards can be proposed (Fig. 15). The ~30.6 Ma obtained for the entire sequence studied would give either (i) a Hauterivian–Albian age, or (ii) the Berriasian–Aptian interval as end-members. Intermediate possibilities are also feasible within the wide age range given by the above-cited authors. In addition, it must be considered that below the studied series there are two syn-rift, post-Kimmeridgian units (Tera and Oncala groups) whose combined thickness is about 3000 m. Our output curve of the 405-kyr cycle filter (Figs. 14 and 15) shows clusters in larger cycles (~2.4 myr), and both show differences in amplitude throughout the stratigraphic succession. In the lower part (cycles 1 to 30, Urbión Group and basal part of the Enciso Group), many cycles have high amplitude, while in the upper part, especially from cycles 31 to 58 (Enciso Group and basal part of the Oliván Group), shorter cycles predominate. These differences in amplitude closely resemble those shown in the 405-kyr Gaussian filter output (centred in 0.002471 ± 0.00024942; band 367–450 Kyr) of the eccentricity numerical solution of Laskar et al. (2011), and they are the basis for the dating of units proposed in this study and for anchoring them to the Geologic Time Scale 2020 (Gale et al., 2020) (Fig. 15). Note that most boundaries between the Early Cretaceous stages still remain unreliably anchored in the GTS2020 and are still under discussion (e.g., Gale et al., 2020; Martinez et al., 2020 and references herein). Indeed, the Global Boundary Stratotype Section and Point (GSSP) for the Barremian Stage (125.77 Ma) has been recently approved (March 2023) by the International

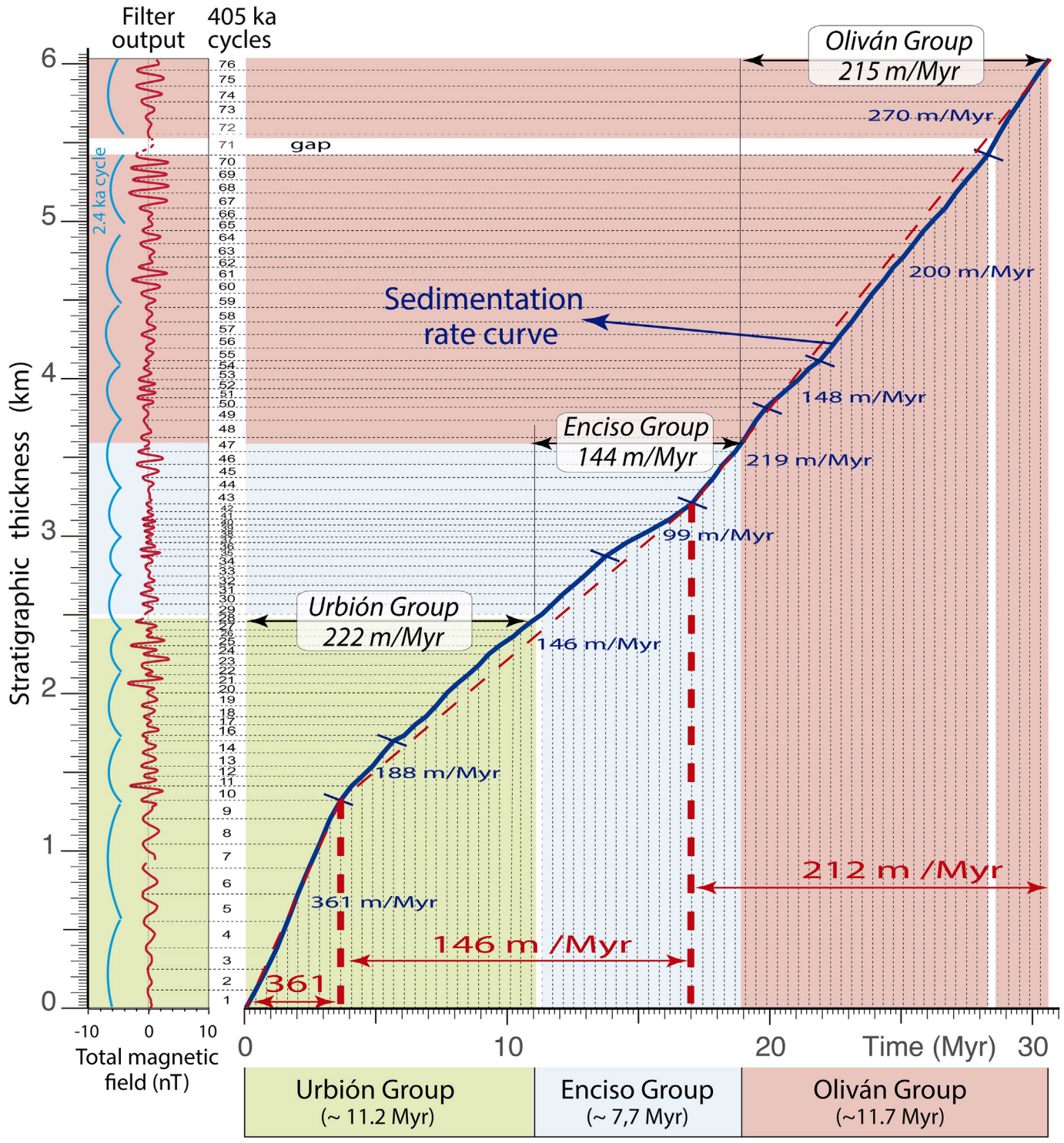

Fig. 14. Filtered output (depth domain) of the time series of the total magnetic field in the Cidacos section (see Fig. 5C), and its plot against time based on the distinguished cycles of large eccentricity (405 kyr). Note that groups of 5–6 (405 kyr) cycles of different amplitude define major cycles that have been related to the 2.4-myr eccentricity cycle. The time lapse for the Urbión, Enciso and Oliván groups is also shown, as well as sedimentation rates (without decompacting the stratigraphic series) for different time intervals (see main text for further explanation).

Union of Geological Sciences (IUGS) Executive Committee and incorporated to the International Chronostratigraphic Chart (Cohen et al., 2013; updated). According to our correlation (Fig. 15), the Cidacos section would span from ~143.2 Ma (Tithonian–Berriasian boundary) to ~112.6 Ma (basalmost Albian), and the base of the Enciso and Oliván groups would be at ~132.1 Ma (basal Hauterivian) and ~124.2 Ma (lower Barremian), respectively. These ages could be carefully extrapolated to the rest of the units of the Cameros basin, honouring transitions and lateral facies changes between them (Muñoz et al., 2020).

The age proposed for the Cidacos section is in agreement with the biostratigraphic ages based on ostracod assemblages (Schudack

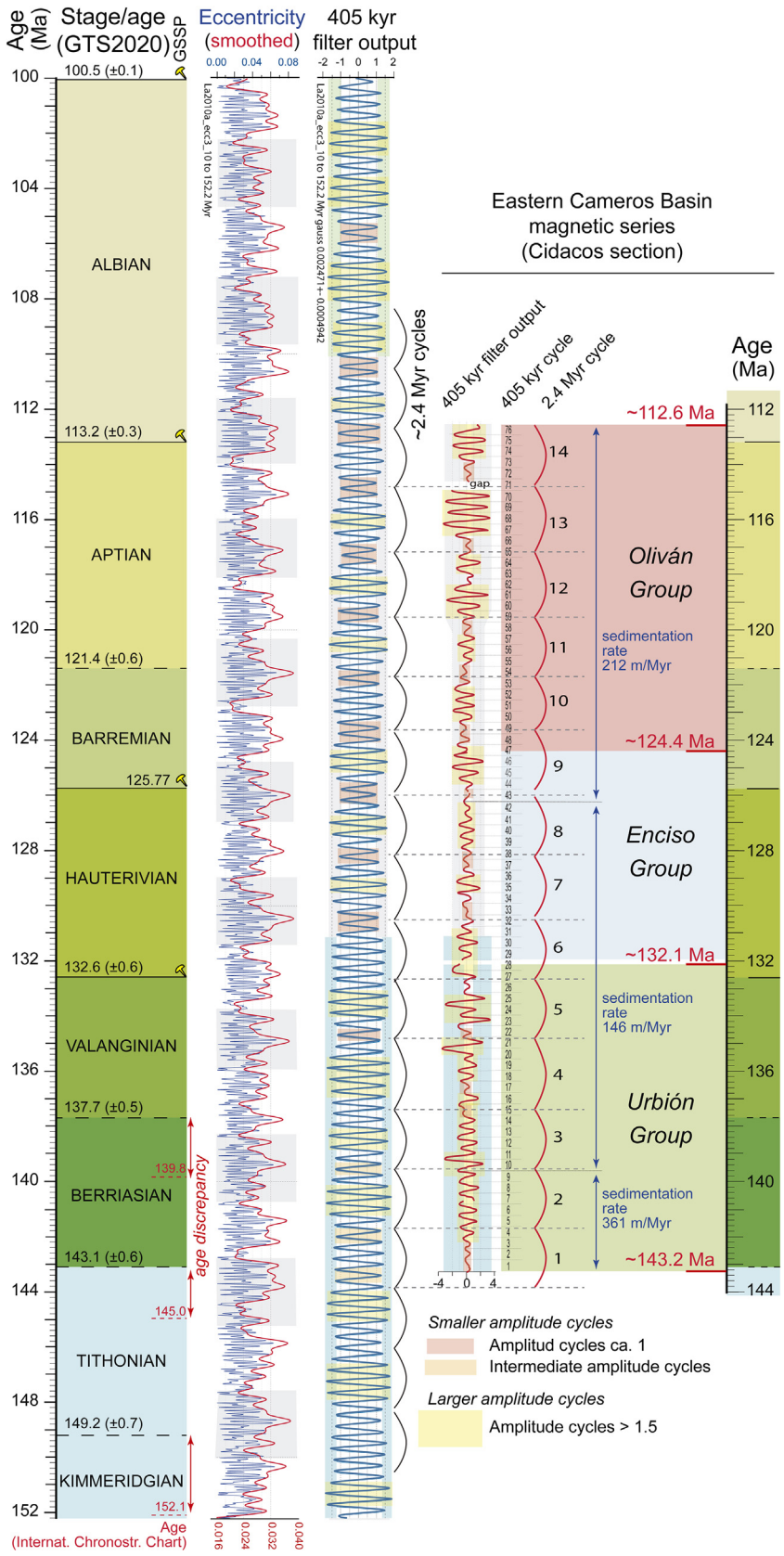

Fig. 15. Proposed dating of the Urbión, Enciso and Oliván groups in the Cidacos section (eastern Cameros Basin) based on the correlation of large (405 kyr) and very large (2.4 myr) eccentricity cycles with the orbital solution for the long-term motion of the Earth from Laskar et al. (2011). The eccentricity data (blue line) and its smoothing (red line) as well as the 405-kyr filter output (centred in 0.002471 ± 0.00024942; band 367–450 Kyr) of the numerical solution Laskar et al. (2011) are shown. Stage ages and age uncertainties based on the Geological Time Scale 2020 (Gale et al., 2020) and the International Chronostratigraphic Chart (Cohen et al., 2013; updated).

and Schudack, 2009). This age pattern and, in particular, the variations in the sedimentation rate, correlate with the rifting stages developed in other significant basins of central-eastern Iberia during the Late Jurassic–Early Cretaceous stage (Liesa et al., 2019 and references therein). Changes of the sedimentation rate and basin evolution have been associated with the opening of the North and Central Atlantic and the Tethys Sea (e.g., Salas and Casas, 1993; Liesa et al., 2019). Backstripped tectonic subsidence of the Maestrazgo (>6000 m of sedimentary rocks) and South Iberian basins at their depocentral areas (Salas and Casas, 1993; Salas et al., 2001), show more precise age determinations, with two main rifting stages (Kimmeridgian–latest Berriasian and late Hauterivian–basal Aptian) separated by a period of decelerating subsidence (Liesa et al., 2006, 2019). These stages match with the three stages with different sedimentation rates defined in this work for the Cameros Basin (361 m/myr, 146 m/myr, and 212 m/myr, Fig. 15). The lowest sedimentation rate interval in the Cameros Basin spans from the late Berriasian to the Hauterivian–Barremian boundary, mimicking the low subsidence period of the other basins. Due to the high sediment supply that was continuously received by the eastern Cameros Basin, the sedimentation rates, and their variations, were probably linked to the tectonic forcing of the normal fault limiting the Cameros Basin to the North. This structure was responsible for the creation of the accommodation space for the basin infill. Therefore, the periods with lower sedimentation rates were likely the result of deceleration phases of fault-related subsidence. In addition, the basal part of the Urbión Group with a high sedimentation rate (361 m/myr) together with the previous 3000-thick synrift deposits (Tera and Oncala groups) would be related to the first rifting stage (Kimmeridgian–Berriasian) described in most basins in central-eastern Iberia (Martín-Chivelet et al., 2019).

7. Conclusions

The application of magnetic surveying (total magnetic field and magnetic gradient) to the study of magnetic susceptibility of sedimentary sequences is a useful tool, provided that certain outcrop and structural conditions of the involved units are met. The magnetic anomalies obtained provide a record of the changes in magnetic susceptibility and/or remanence of the outcropping units, and hence of their iron content, that can be related to climatic changes.

Cyclicity established on this basis for the total magnetic field gives results that are consistent with cycles in the frequency bands of 700–350 m, 150–80 m, 50–20 m, 20–8 m, and 10–4 m. They are interpreted to represent the cycles of very large (2.4 myr), large (405 kyr) and short eccentricity (100–125 kyr), obliquity (40 kyr) and precession (19–23 kyr), respectively. Seventy-six cycles of large eccentricity, with a total duration of ~30.6 million years, and a mean sedimentation rate of 0.2 mm/yr, are interpreted for the 6070 thick sedimentary succession. Broad frequency bands result from changing sedimentation rates, ranging from 0.1 mm/yr to >3.5 mm/yr. Differences in the amplitude of the 405-kyr cycles and their arrangement along the succession have been used for anchoring the series to the orbital solution of eccentricity cycles and to the Geologic Time Scale 2020. The whole Cidacos section spans from the Tithonian–Berriasian boundary (~143.2 Ma) to the basalmost Albian (~112.6 Ma), and shows two periods of high sedimentation rate separated with a period (late Berriasian to Hauterivian–Barremian boundary) of lower sedimentation rate. These three stages correlate well with the tectonic subsidence analysis of the main Early Cretaceous basins in central-eastern Iberia, reinforcing the proposed dating of the Cameros basin infill.

The routine for the application of this magnetic survey technique for cyclostratigraphic purposes is relatively simple and presents the advantages of a higher number of measurements, higher representativeness, quick data acquisition, and the possibility of surveying non-exposed units. This minimizes gaps in the magnetic records. Our results also contribute significantly to the validation of the use of these climatic-driven parameters (total magnetic field and gradient), in combination with cyclicity analyses, for their indirect use in astrochronological dating.

Funding

This work was supported by the Agencia Estatal de Investigación (AEI/10.13039/501100011033) of the Spanish Government (projects PID2019-108753GB-C22 and PID2019-108705GB-I00), and the Gobierno de Aragón (E32_23R: Geotransfer Research Group).

Data availability

The raw data supporting the conclusions of this article are available in the Mendeley data repository (https://data.mendeley.com/datasets/vm8kbhc7s6/1).

Acknowledgements

We express our sincere thanks to Francesca Loi for her help in collecting data in the field. The authors thank the editor and an anonymous referee for their help and suggestions.

References

Angulo, A., Muñoz, A., 2013. Análisis de la periodicidad climática de baja frecuencia registrada en los sedimentos lacustres del Grupo Enciso (Cretácico Inferior de la cuenca de Cameros, La Rioja): Aplicaciones a la correlación y datación de la serie. Boletin Geologico y Minero 124, 203–219. https://www.igme.es/boletin/2013/124_2/8_ARTICULO%205.pdf.

Barrenechea, J.F., Rodas, M., Frey, M., Alonso-Azcárate, J., Mas, J.R., 2000. Chlorite, corrensite, and chlorite-mica in late Jurassic fluvio-lacustrine sediments of the Cameros basin of northeastern Spain. Clays and Clay Minerals 48, 256–265.

Boulila, S., Galbrun, B., Hinnov, L.A., Collin, P.Y., 2008. High-resolution cyclostratigraphic analysis from magnetic susceptibility in a Lower Kimmeridgian (Upper Jurassic) marl–limestone succession (La Méouge, Vocontian Basin, France). Sedimentary Geology 203, 54–63. https://doi.org/10.1016/j.sedgeo.2007.10.004.

Brenner, P., 1976. Ostracoden und charophyten des spanischen Wealden (Systematik. Oekologie. Stratigraphie. Palaeogeographie). Palaeontographica Abt.A. 152 (4–6), 113–201.

Brocke, R., Brett, C.E., Ellwood, B.B., Hartkopf-Fröder, C., Riegel, W., Schindler, E., Tomkin, J.H., 2017. Comparative palynofacies, magnetic susceptibility and cyclicity of the Middle Devonian Müllertchen Section (Eifel area, Germany). Palaeobiodiversity and Palaeoenvironments 97 (3), 449–467. https://doi.org/10.1007/s12549-017-0289-9.

Butler, D.K., 2005. Near-surface Geophysics. Society of Exploration Geophysics.

Burger, H.R., Sheehan, A.F., Jones, C.H., Burger, H.R., 2006. Introduction to Applied Geophysics: Exploring the Shallow Subsurface, vol. 550. W. W. Norton, New York.

Calvín, P., Casas, A.M., Villalaín, J.J., Tierz, P., 2014. Reverse magnetic anomaly controlled by Permian Igneous rocks in the Iberian Chain (N Spain). Geológica Acta 12, 193–207.

Casas, A.M., Villalaín, J.J., Soto, R., Gil-Imaz, A., Del Río, P., Fernández, G., 2009. Multidisciplinary approach to an extensional syncline model for the Mesozoic Cameros Basin (N Spain). Tectonophysics 470, 3–20. https://doi.org/10.1016/j.tecto.2008.04.020.

Casas, A.M., Del Río, P., Mata, P., Villalaín, J., Barbero, L., 2012. Comment on González-Acebrón et al. Criteria for the recognition of localization and timing of multiple events of hydrothermal alteration in sandstones illustrated by petrographic, fluid inclusion, and isotopic analysis of the Tera Group, Northern Spain Int. J. Earth Sci. (2011) 100: 1811–1826. International Journal of Earth Sciences 101, 2043–2048.

Casas Sainz, A.M., 1993. Oblique tectonic inversion and basement thrusting in the Cameros Massif (Northern Spain). Geodinamica Acta 6 (3), 202–216. https://doi.org/10.1080/09853111.1993.11105248.

Casas-Sainz, A.M., Gil-Imaz, A., 1998. Extensional subsidence, contractional folding and thrust inversion of the eastern Cameros basin, northern Spain. Geologische Rundschau 86, 802–818. https://doi.org/10.1007/s005310050178.

Casas-Sainz, A.M., Santolaria, P., Mochales, T., Pocoví, A., Izquierdo, E., El-Ouardi, H., Moussaid, B., Manar, A., Ruiz-Martínez, V.C., Torres-López, S., Gil-Imaz, A., Román-Berdiel, T., Oliva, B., Calvín, P., 2023. Structure of the Central High Atlas (Morocco). Constraints from Potential Field Data and 3D Models. In: Tectonic Evolution of the Moroccan High Atlas: a Paleomagnetic Perspective: Magnetic Techniques (Anisotropy of Magnetic Susceptibility and Paleomagnetism)

Applied to the Understanding of the Evolution of an Intra-Plate Mountain Chain. Springer International Publishing, Cham, pp. 75–247.
Clemente, P., 2010. Review of the upper Jurassic-lower Cretaceous stratigraphy in western Cameros Basin, Northern Spain. Revista de la Sociedad Geologica de Espana 23, 101–143. https://sge.usal.es/archivos/REV/23(3-4)/art03.pdf.
Cleveland, W.S., 1981. LOWESS: A program for smoothing scatterplots by robust locally weighted regression. The American Statistician 35, 54. https://doi.org/10.2307/2683591.
Cohen, K.M., Finney, S.C., Gibbard, P.L., Fan, J.-X., 2013. updated. The ICS International Chronostratigraphic Chart. Episodes 36, 199–204.
Collinson, D.W., 1967. The variation of magnetic properties among red sandstones. Geophysical Journal International 12 (2), 197–207.
Da Silva, A.C., De Vleeschouwer, D., Boulvain, F., Claeys, P., Fagel, N., Humblet, M., Mabille, C., Michel, J., Sardar Abadi, M., Pas, D., Dekkers, M.J., 2013. Magnetic susceptibility as a high-resolution correlation tool and as a climatic proxy in Paleozoic rocks – merits and pitfalls: examples from the Devonian in Belgium. Marine and Petroleum Geology 46, 173–189. https://doi.org/10.1016/j.marpetgeo.2013.06.012.
Del Río, P., Casas, A., Villalaín, J.J., Mochales, T., Soto, R., Oliva-Urcia, B., 2013. Interpretation of gravimetric and magnetic anomalies in the Cameros Basin (North Spain): combination of deep and shallow sources. Studia Geophysica et Geodaetica 57, 442–459. https://doi.org/10.1007/s11200-012-0369-2.
Dentith, M.C., Mudge, S., 2014. Geophysics for the Mineral Exploration Geoscientist. Cambridge University Press.
Dentith, M., Enkin, R.J., Morris, W., Adams, C., Bourne, B., 2020. Petrophysics and mineral exploration: a workflow for data analysis and a new interpretation framework. Geophysical Prospecting 68 (1-Cost-Effective and Innovative Mineral Exploration Solutions), 178–199.
Dietze, F., Kontny, A., Heyde, I., Vahle, C., 2011. Magnetic anomalies and rock magnetism of basalts from Reykjanes (SW-Iceland). Studia Geophysica et Geodaetica 55, 109–130.
Doublet, S., 2004. Contrôles tectonique et climatique de l'enregistrement stratigraphique dans un bassin continental de rift: le bassin de Cameros (Jurassique supérieur-Crétacé inférieur) provinces de Soria-La Rioja, Espagne (PhD Thesis). Université de Bourgogne, Centre des Sciences de la Terre, Bourgogne, p. 497.
Doublet, S., García, J.P., Guiraud, M., Menard, A., 2003. Wave dominated siliciclastic and carbonate sedimentation in a Lower Cretaceous lake (Cameros basin, northern Spain). Journal of Iberian Geology 29, 11–30.
Ellwood, B.B., Crick, R.E., El Hassani, A., Benoist, S.L., Young, R.H., 2000. Magnetosusceptibility event and cyclostratigraphy method applied to marine rocks: detrital input versus carbonate productivity. Geology 28, 1135–1138. https://doi.org/10.1130/0091-7613(2000)28<1135:MEACMA>2.0.CO;2.
Eppelbaum, L.V., 2019. Geophysical Potential Fields: Geological and Environmental Applications. In: Computational Geophysics Series, vol. 2. Elsevier.
Everett, M.E., 2013. Near-surface Applied Geophysics. Cambridge University Press.
Florsch, N., Camerlynck, C., Kammenthaler, M., Muhlach, F., 2018. Everyday Applied Geophysics 2: Electromagnetics and Magnetics. ISTE Press Limited-Elsevier Incorporated.
Gadallah, M.R., Fisher, R., 2008. Exploration Geophysics. Springer Science & Business Media.
Gale, A.S., Mutterlose, J., Battenburg, S., Gradstein, F.M., Agterberg, J.G., Ogg, J.G., Petrizzo, M.R., 2020. The Cretaceous period. In: Gradstein, F.M., Ogg, J.G., Schmitz, M.D., Ogg, G.M. (Eds.), The Geological Time Scale 2020, vol. 2. Elsevier, pp. 1023–1086. https://doi.org/10.1016/B978-0-12-824360-2.00027-9. https://doi.org/10.1016/C2020-1-02369-3.
García-Lasanta, C., Oliva-Urcia, B., Román-Berdiel, T., Casas, A.M., Pérez-Lorente, F., 2013. Development of magnetic fabric in sedimentary rocks: insights from early compactional structures. Geophysical Journal International 194, 182–199. https://doi.org/10.1093/gji/ggt098.
García-Lasanta, C., Oliva-Urcia, B., Román-Berdiel, T., Casas, A.M., Hirt, A.M., 2014. Understanding the Mesozoic kinematic evolution in the Cameros basin (Iberian Range, NE Spain) from magnetic subfabrics and mesostructures. Journal of Structural Geology 66, 84–101. https://doi.org/10.1016/j.jsg.2014.05.013.
García-Lasanta, C., Casas-Sainz, A., Villalaín, J.J., Oliva-Urcia, B., Mochales, T., Speranza, F., 2017. Remagnetizations used to unravel large-scale fold kinematics: A case study in the Cameros Basin (Northern Spain). Tectonics 36, 714–729. https://doi.org/10.1002/2016TC004459.
Gil-Imaz, A., Pocoví, A., Lago, M., Parés, J.M., 2000. Effect of lithostatic pressure and tectonic deformation on the magnetic fabric (anisotropy of magnetic susceptibility) in low-grade metamorphic rocks. Journal of Geophysical Research: Solid Earth 105 (B9), 21305–21317. https://doi.org/10.1029/2000JB900171.
Goldberg, J.M., Guiraud, M., Maluski, H., Séguret, M., 1988. Caractères pétrologiques et âge du métamorphisme en contexte distensif du bassin sur décrochement de Soria (Crétacé inférieur, Nord Espagne). Comptes Rendus de l'Academie des Sciences 307, 521–527.
Golovanova, I.V., Danukalov, K.N., Salmanova, R.Y., Levashova, N.M., Parfiriev, N.P., Sergeeva, N.D., Meert, J.G., 2023. Magnetic field hyperactivity during the early Neoproterozoic: A paleomagnetic and cyclostratigraphic study of the Katav Formation, southern Urals, Russia. Geoscience Frontiers 14, 101558. https://doi.org/10.1016/j.gsf.2023.101558.
Gracia-Puzo, F., Aubourg, C., Casas-Sainz, A., 2021. A fast way to estimate the clay fabric from shale fragments. Key example from a strained footwall (Pyrenees). Journal of Structural Geology 152, 104443. https://doi.org/10.1016/j.jsg.2021.104443.
Griffiths, D.H., King, R.F., 2013. Applied Geophysics for Geologists and Engineers: The Elements of Geophysical Prospecting. Elsevier.
Guimerà, J., Alonso, Á., Mas, J.R., 1995. Inversion of an extensional-ramp basin by a newly formed thrust: the Cameros basin (N. Spain). Geological Society, London, Special Publications 88, 433–453. https://doi.org/10.1144/GSL.SP.1995.088.01.23.
Guiraud, M., Séguret, M., 1985. A releasing solitary overstep model for the late Jurassic-early Cretaceous (Wealdian) Soria strike-slip basin (Northern Spain). In: Biddle, K.T., Christie-Blick, N. (Eds.), Strike-Slip Deformation, Basin Formation, and Sedimentation, Special Publication of the Society of Economic, Paleontologists and Mineralogists (SEPM), vol. 37, pp. 159–175.
Gunderson, K.L., Kodama, K.P., Anastasio, D.J., Pazzaglia, F.J., 2013. Rock-magnetic cyclostratigraphy for the Late Pliocene–Early Pleistocene Stirone section, Northern Apennine mountain front, Italy. Geological Society, London, Special Publications 373, 309–323.
Hernán, J., 2018. Estratigrafía y sedimentología de las formaciones con icnitas de dinosaurios del Grupo Enciso (Cameros, La Rioja, Aptiense) (PhD thesis). Universidad Politécnica de Madrid, p. 521.
Hinnov, L.A., 2013. Cyclostratigraphy and its revolutionizing applications in the Earth and Planetary Sciences. Bulletin of the Geological Society of America 125, 1703–1734. https://doi.org/10.1130/B30934.1.
Hinze, W.J., Von Frese, R.R., Von Frese, R., Saad, A.H., 2013. Gravity and Magnetic Exploration: Principles, Practices, and Applications. Cambridge University Press. https://doi.org/10.1017/CBO9780511843129.
Hrvoic, I., 1990. Proton magnetometers for measurement of the Earth's magnetic field. In: Proc. Int. Workshop Geomagn. Observatory Data Acquisition Process, pp. 103–109.
Jelínek, V., 1977. The Statistical Theory of Measuring Anisotropy of Magnetic Susceptibility of Rocks and Its Application, vol. 29. Geofyzika, Brno, Czech Republic, pp. 1–87.
Kearey, P., Brooks, M., Hill, I., 2002. An Introduction to Geophysical Exploration, third ed. Blackwell Publishing Company.
Kneuper-Haack, F., 1966. Ostracoden aus dem Wealden der Sierra de los Cameros (Nordwestliche Iberische Ketten). Beihefte Geologisches Jahrbuch 44, 165–209.
Kodama, K.P., Hinnov, L.A., 2014. Rock Magnetic Cyclostratigraphy. John Wiley and Sons, Ltd., Oxford https://doi.org/10.1002/9781118561294.
Kodama, K.P., Hinnov, L.A., 2015. Rock Magnetic Cyclostratigraphy. Wiley-Blackwell, Oxford, p. 176.
Kodama, K.P., Anastasio, D.J., Newton, M.L., Pares, J.M., Hinnov, L.A., 2010. High-resolution rock magnetic cyclostratigraphy in an Eocene flysch, Spanish Pyrenees. Geochemistry, Geophysics, Geosystems 11 (6), Q0AA07. https://doi.org/10.1029/2010GC003069.
Koptíková, L., Bábek, O., Hladil, J., Kalvoda, J., Slavík, L., 2010. Stratigraphic significance and resolution of spectral reflectance logs in Lower Devonian carbonates of the Barrandian area, Czech Republic; a correlation with magnetic susceptibility and gamma-ray logs. Sedimentary Geology 225, 83–98. https://doi.org/10.1016/J.SEDGEO.2010.01.004.
Laskar, J., Robutel, P., Joutel, F., Gastineau, M., Correia, A.C.M., Levrard, B., 2004. A long-term numerical solution for the insolation quantities of the Earth. Astronomy & Astrophysics 428, 261–285. https://doi.org/10.1051/0004-6361:20041335.
Laskar, J., Fienga, A., Gastineau, M., Manche, H., 2011. La2010: a new orbital solution for the long-term motion of the Earth. Astronomy & Astrophysics 532, A89. https://doi.org/10.1051/0004-6361/201116836.
Li, M., Hinnov, L., Kump, L., 2019. Acycle: Time-series analysis software for paleoclimate research and education. Computers & Geosciences 127, 12–22. https://doi.org/10.1016/j.cageo.2019.02.011.
Liesa, C.L., Soria, A.R., Meléndez, N., Meléndez, A., 2006. Extensional fault control on the sedimentation patterns in a continental rift basin: El Castellar Formation, Galve sub-basin, Spain. Journal of the Geological Society of London 163, 487–498. https://doi.org/10.1144/0016-764904-169.
Liesa, C.L., Casas, A.M., Simón, J.L., 2018. La tectónica de inversión en una región intraplaca: la Cordillera Ibérica. Revista de la Sociedad Geologica de Espana 31, 23–50. https://sge.usal.es/archivos/REV/31(2)/RSGE3 1(2)_p_23_50.pdf.
Liesa, C.L., Soria, A.R., Casas, A., Aurell, M., Meléndez, N., Bádenas, B., Fregenal-Martínez, M., Navarrete, R., Peropadre, C., Rodríguez-López, J.P., 2019. The south-Iberian, central Iberian and Maestrazgo basins. In: Oliveira, J.T., Quesada, C. (Eds.), The geology of Iberia: A geodynamic approach, Regional Geology Reviews, vol. 3. Springer Nature, pp. 214–228 (the Alpine cycle, Chapter 5; Late Jurassic-Early Cretaceous rifting).
Liesa, C.L., Casas, A., Muñoz, A., Tella, A., 2023. Raw data of "magnetic surveying as a proxy for defining cyclicity in thick sedimentary fillings: application to the Cretaceous Cameros Basin (N Spain)". In: Casas, A.M., Muñoz, A., Tella, A., Liesa, C.L. (Eds.), Mendeley Data, V1. https://doi.org/10.17632/vm8kbhc7s6.1.
Liu, H., Dong, H., Liu, Z., Ge, J., Bai, B., Zhang, C., 2017. Construction of an Overhauser magnetic gradiometer and the applications in geomagnetic observation and ferromagnetic target localization. Journal of Instrumentation 12 (10), T10008.
Liu, W., Wu, H., Hinnov, L.A., Xi, D., He, H., Zhang, S., Yang, T., 2020. Early Cretaceous Terrestrial Milankovitch Cycles in the Luanping Basin, North China and Time Constraints on Early Stage Jehol Biota Evolution. Frontiers in Earth Science 8, 178. https://doi.org/10.3389/feart.2020.00178.

López-Gómez, J., Alonso-Azcárate, J., Arche, A., Arribas, J., Fernández Barrenechea, J., Borruel-Abadía, V., Bourquin, S., Cadenas, P., Cuevas, J., De la Horra, R., Díez, J.B., Escudero-Mozo, M.J., Fernández-Viejo, G., Galán-Abellán, B., Galé, C., Gaspar-Escribano, J., Gisbert Aguilar, J., Gómez-Gras, D., Goy, A., Gretter, N., Heredia-Carballo, N., Lago, M., Lloret, J., Luque, J., Márquez, L., Márquez-Aliaga, A., Martín-Algarra, A., Martín-Chivelet, J., Martín-González, F., Marzo, M., Mercedes-Martín, R., Ortí, F., Pérez-López, A., Pérez-Valera, F., Pérez-Valera, J., Plasencia, P., Ramos, E., Rodríguez-Méndez, L., Ronchi, A., Salas, R., Sánchez-Fernández, D., Sánchez-Moya, Y., Sopeña, A., Suárez-Rodríguez, A., Tubía, J.M., Ubide, T., Valero-Garcés, B., Vargas, H., Viseras, C., 2019. Permian-Triassic rifting stage. In: Oliveira, J.T., Quesada, C. (Eds.), The Geology of Iberia: A Geodynamic Approach, Regional Geology Reviews, vol. 3. The Alpine Cycle, pp. 29–112.

Mann, M.E., Lees, J.M., 1996. Robust estimation of background noise and signal detection in climatic time series. Climate Change 33, 409–445. https://doi.org/10.1007/BF00142586.

Martín-Chivelet, J., López-Gómez, J., Aguado, R., Arias, C., Arribas, J., Arribas, M.E., Aurell, M., Bádenas, B., Benito, M.I., Bover-Arnal, T., Casas-Sainz, A., Castro, J.M., Coruña, F., de Gea, G.A., Fornós, J.J., Fregenal-Martínez, M., García-Senz, J., Garófano, D., Gelabert, B., Giménez, J., González-Acebrón, L., Guimerà, J., Liesa, C.L., Mas, R., Meléndez, N., Molina, J.M., Muñoz, J.A., Navarrete, R., Nebot, M., Nieto, L.M., Omodeo-Salé, S., Pedrera, A., Peropadre, C., Quijada, I.E., Quijano, M.L., Reolid, M., Robador, A., Rodríguez-López, J.P., Rodríguez-Perea, A., Rosales, I., Ruiz-Ortiz, P.A., Sàbat, F., Salas, R., Soria, A.R., Suarez-Gonzalez, P., Vilas, L., 2019. The Late Jurassic–Early Cretaceous rifting (chap. 5). In: Quesada, C., Oliveira, J. (Eds.), The Geology of Iberia: A Geodynamic Approach. Regional Geology Reviews. Springer, Cham, pp. 169–249. https://doi.org/10.1007/978-3-030-11295-0_5.

Martín-Closas, C., 1989. Els carofits del Cretaci inferior de les conques periferiques del Bloc de l'Ebre (PhD thesis). Universitat de Barcelona, p. 581.

Martin-Closas, C., 2000. Els carofits del Jurassic superior i el Cretaci inferior de la Peninsula Iberica. In: Upper Jurassic and Lower Cretaceous Charophytes from the Iberian Peninsula, vol. 125. Arxius de los Seccions de Ciencies, Barcelona, p. 304.

Martín-Closas, C., Alonso Millán, A., 1998. Estratigrafía y bioestratigrafía (Charophyta) del Cretácico Inferior en el sector occidental de la Cuenca de Cameros (Cordillera Ibérica). Revista de la Sociedad Geologica de Espana 11, 253–270. https://sge.usal.es/archivos/REV/11(3-4)/Art05.pdf.

Martinez, M., Aguado, R., Company, M., Sandoval, J., O'Dogherty, L., 2020. Integrated astrochronology of the Barremian Stage (Early Cretaceous) and its biostratigraphic subdivisions. Global and Planetary Change 195, 103368. https://doi.org/10.1016/j.gloplacha.2020.103368.

Mas, R., Benito, M.I., Arribas, J., Serrano, A., Guimerà, J., Alonso, A., Alonso-Azcárate, J., 2002. La Cuenca de Cameros: desde la extensión finijurásica-eocretácica a la inversión terciaria-implicaciones en la exploración de hidrocarburos. Zubia – Monografico 14, 9–64.

Mata, M.P., Prieto, A.C., Rull, F., Alia, J.M., López-Aguayo, F., 1991. Cloritas dioctaédricas asociadas a piritas en metapelitas de la Sierra de los Cameros. Estudios Geológicos 47 (3–4), 129–135.

Mata, M.P., Casas, A.M., Canals, A., Gil, A., Pocovi, A., 2001. Thermal history during Mesozoic extension and Tertiary uplift in the Cameros Basin, northern Spain. Basin Research 13, 91–111. https://doi.org/10.1046/j.1365-2117.2001.00138.x.

Mata-Campo, M.P., 1997. Caracterización y evolución mineralógica de la cuenca mesozoica de Cameros (Soria – La Rioja) (Ph. D. thesis). University of Zaragoza, p. 350.

Mata-Campo, M.P., López-Aguayo, F., 2002. La cookeita asociada a la pinta de la Cuenca de Cameros: estudio por microscopía electrónica de barrido y transmisión. Zubia (14), 155–172.

Milankovitch, M.M., 1941. Canon of insolation and the iceage problem. Koniglich Serbische Akademice Beograd Special Publication, p. 132.

Milsom, J., 2003. Field Geophysics, third ed. John Willey and Sons.

Moreno-Azanza, M., Gasca, J.M., Díaz-Martínez, I., Lázaro, B.B., Fernández, A., Pérez-Lorente, F., 2020. A multi-ootaxic assemblage from the Lower Cretaceous of the Cameros Basin (La Rioja; northern Spain). Spanish Journal of Palaeontology 31, 305–320. https://doi.org/10.7203/sjp.31.2.17158.

Muñoz, A., Angulo, A., Liesa, C.L., Luzón, M.A., Mayayo, M.J., Pérez, A., Soria, A.R., Val, V., Yuste, A., 2020. Periodicidad climática y datación astrocronológica del Grupo Enciso en la cuenca oriental de Cameros (N de España). Boletin Geologico y Minero 131, 243–268. https://doi.org/10.21701/bolgeomin.131.2.003.

Muñoz, A., Angulo, A., Liesa, C.L., Luzón, M.A., Mayayo, M.J., Pérez, A., Soria, A.R., Val, V., Yuste, A., 2021. Cicloestratigrafía del Grupo Enciso. Cuenca oriental de Cameros (N de España). In: X Congreso Geológico de España (Vitoria, España), vol. 18. Geo-Temas, p. 173.

Muñoz-Jiménez, A., Casas-Sainz, A.M., 1997. The Rioja Trough (N Spain): tectosedimentary evolution of a symmetric foreland basin. Basin Research 9, 65–85. https://doi.org/10.1046/j.1365-2117.1997.00031.x.

Muñoz Jiménez, A., Soria de Miguel, A.R., Canudo Sanagustín, J.I., Casas Sainz, A.M., Gil Imaz, A., Mata Campo, M.P., 1997. Caracterización estratigráfica y sedimentológica del Albiense marino del borde Norte de la Sierra de Cameros: Implicaciones paleogeográficas. Cuadernos de Geología Ibérica 22, 139–164.

Oliva-Urcía, B., Muñoz, A., Larrasoaña, J.C., Luzón, A., Pérez, A., González, A., Jianz, S., Liu, Q., Román-Berdiel, T., 2016. Response of alluvial systems to Late Pleistocene climate changes recorded by environmental magnetism in the Añavieja Basin (Iberian Range, NE Spain). Geológica Acta 14, 139–154.

Omar, H., Da Silva, A.-C., Yaich, C., 2021. Linking the variation of sediment accumulation rate to short term sea-level change using cyclostratigraphy: Case study of the lower Berriasian hemipelagic sediments in Central Tunisia (southern Tethys). Frontiers in Earth Science 9, 638441. https://doi.org/10.3389/feart.2021.638441.

Omodeo Salè, S., Guimerà, J., Mas, R., Arribas, J., 2014. Tectono-stratigraphic evolution of an inverted extensional basin: the Cameros Basin (north of Spain). International Journal of Earth Sciences 103, 1597–1620. https://doi.org/10.1007/s00531-014-1026-5.

Oswin, J., 2009. A Field Guide to Geophysics in Archaeology. Springer Science & Business Media.

Pedley, R.C., Busby, J.P., Dabek, Z.K., 1993. GRAVMAG User Manual. British Geological Survey. Keyworth, Nottingham.

Pfeifer, L.S., Hinnov, L., Zeeden, C., Rolf, C., Laag, C., Soreghan, G.S., 2020. Rock magnetic cyclostratigraphy of Permian loess in eastern Equatorial Pangea (Salagou Formation, South-Central France). Frontiers in Earth Science 8, 241. https://doi.org/10.3389/feart.2020.00241.

Powers, M.C., Anastasio, D.J., Parés, J.M., Duval, M., Kodama, K.P., 2020. High resolution chronology using rock magnetic cyclostratigraphy in the Baza basin, Southern Spain. In: Joint 69th Annual Southeastern/55th Annual Northeastern Section Meeting – 2020. Geological Society of America Abstracts with Programs, vol. 52(2). https://doi.org/10.1130/abs/2020SE-344970.

Pueyo Anchuela, Ó., Diarte Blasco, P., García Benito, C., Casas Sainz, A.M., Pocoví Juan, A., 2016. Geophysical and archaeological characterization of a modest roman villa: methodological considerations about progressive feedback analyses in sites with low geophysical contrast. Archaeological Prospection 23, 105–123. https://doi.org/10.1002/arp.1529.

Salas, R., Casas, A., 1993. Mesozoic extensional tectonics, stratigraphy and crustal evolution during the Alpine cycle of the eastern Iberian basin. Tectonophysics 228, 33–55. https://doi.org/10.1016/0040-1951(93)90213-4.

Salas, R., Guimerà, J., Mas, R., Martín-Closas, C., Meléndez, A., Alonso, A., 2001. Evolution of the Mesozoic Central Iberian Rift System and its Cenozoic inversion (Iberian Chain). In: Ziegler, P.A., Cavazza, W., Robertson, A.H.F., Crasquin-Soleau, S. (Eds.), Peri-Tethys Memoir 6: Peri-Tethyan Rift/Wrench Basins and Passive Margins, Mémoires du Muséum National d'Histoire Naturelle, vol. 186, pp. 145–185.

Salomon, J.N., 1982. Les formations continentales du bassin de Soria (Sierra de los Cameros) au Jurassique Supérieur-Crétacé inférieur: relation entre tectonique et sédimentation. Cuadernos de Geología Ibérica 8, 167–186.

Schlicht, P., Koutsoukos, E.A.M., Hambach, U., Bengtson, P., Krumsiek, K., 1998. Magnetic properties of Maastrichtian to Paleocene sediments from the Pernambuco–Paraíba Basin (NE Brazil): preliminary results. In: South Atlantic Mesozoic Correlations, SAMC – Project 381 (IGCP-IUGS), Abstracts of the Third Annual Conference, Comodoro Rivadavia–Ushuaia, November 1998. Boletín de la Asociación Paleontológica del Golfo de San Jorge 2 (Special Edition), pp. 29–30.

Schlicht, P., Bengtson, P., Hambach, U., Krumsiek, K., Koutsoukos, E.A.M., 1999. Limestone-marl cycles from the Maastrichtian of the Pernambuco-Paraíba Basin (NE Brazil) – evidence for orbital forcing? In: Dias-Brito, D., Castro, J.C., Rohn, R. (Eds.), Boletim do V Simpósio sobre o Cretáceo do Brasil & I Simposio sobre el Cretácico de América del Sur (Serra Negra-SP, 29/08-02/09/99), pp. 121–124.

Schudack, M., 1987. Charophytenflora und fazielle Entwick-lung der Grenzschichten mariner Jura/Wealden in den Nord-westlichen Iberischen Ketten (mit Vergleichen zu Asturien und Kantabrien). Palaeontographica B 204, 1–180.

Schudack, U., Schudack, M., 2009. Ostracod biostratigraphy in the Lower Cretaceous of the Iberian chain (eastern Spain). Journal of Iberian Geology 35, 141–168.

Schudack, M., Schudack, U., 2011. Ostracod associations (marine and nonmarine) from the Lower Cretaceous of the Iberian chain (eastern Spain) and their biostratigraphical potential. Joannea – Geologie und Paläontologie 11, 185–188.

Singsoupho, S., Bhongsuwan, T., Elming, S.Å., 2015. Palaeocurrent direction estimated in Mesozoic redbeds of the Khorat Plateau, Lao PDR, Indochina Block using anisotropy of magnetic susceptibility. Journal of Asian Earth Sciences 106, 1–18.

Smekalova, T.N., Voss, O., Smekalov, S.L., 2008. Magnetic surveying in archaeology, 2nd revised edition. In: More than 10 years of using the Overhauser GSM-19 gradiometer. Wormianum, Denmark.

Soto, R., Casas-Sainz, A.M., Del Río, P., 2007. Geometry of half-grabens containing a mid-level viscous décollement. Basin Research 19, 437–450. https://doi.org/10.1111/j.1365-2117.2007.00328.x.

Soto, R., Villalaín, J.J., Casas-Sainz, A.M., 2008. Remagnetizations as a tool to analyze the tectonic history of inverted sedimentary basins: A case study from the Basque-Cantabrian basin (north Spain). Tectonics 27. https://doi.org/10.1029/2007TC002208.

Stage, M., 2001. Magnetic susceptibility as carrier of a climatic signal in chalk. Earth and Planetary Science Letters 188, 17–27. https://doi.org/10.1016/S0012-821X(01)00304-1.

Telford, W.M., Telford, W.M., Geldart, L.P., Sheriff, R.E., 1990. Applied Geophysics. Cambridge University Press.

Tischer, G., 1966a. Über die Wealden-Ablagerung und die Tek-tonik der östlichen Sierra de los Cameros (Spanien). Beihefte Geologisches Jahrbuch 44, 123–164.

Tischer, G., 1966b. El delta Weáldico de las montañas Ibéricas Occidentales y sus enlaces tectónicos. In: Not. Com., vol. 81. Instituto Geológico y Minero de España, pp. 53–78.

Thomson, D.J., 1982. Spectrum estimation and harmonic analysis. Proceedings of the IEEE 70, 1055–1096.

Torres-López, S., Casas, A.M., Villalaín, J.J., El Ouardi, H., Moussaid, B., 2016. Pre-Cenomanian vs. Cenozoic folding in the High Atlas revealed by palaeomagnetic data. Terra Nova 28, 110–119. https://doi.org/10.1111/ter.12197.

Vandenberghe, J., Lu, H., Sun, D., van Huissteden, J.K., Konert, M., 2004. The late Miocene and Pliocene climate in East Asia as recorded by grain size and magnetic susceptibility of the Red Clay deposits (Chinese Loess Plateau). Palaeogeography, Palaeoclimatology, Palaeoecology 204, 239–255. https://doi.org/10.1016/S0031-0182(03)00729-6.

Villalaín, J.J., Fernández-González, G., Casas, A.M., Gil-Imaz, A., 2003. Evidence of a Cretaceous remagnetization in the Cameros Basin (North Spain): implications for basin geometry. Tectonophysics 377, 101–117. https://doi.org/10.1016/j.tecto.2003.08.024.

Witten, A.J., 2006. Handbook of Geophysics and Archaeology. Equinox Publish, London.

Appendix A. Supplementary data

Supplementary data to this article can be found online at https://doi.org/10.1016/j.cretres.2023.105736.